

Aerothermodynamics of the Mars Global Surveyor
Spacecraft



By
Russell William Shane
BS. Aerospace Engineering, University of California, Los Angeles,
December 1992

A Thesis submitted to

The Faculty of

The School of Engineering and Applied Science
of the George Washington University in partial satisfaction
of the requirements for the degree of Master of Science

December 1997

Thesis directed by
Dr. Robert H. Tolson
Professor of Engineering and Applied Science

This research was conducted at NASA Langley Research Center

Abstract

The aerothermodynamic characteristics of the Mars Global Surveyor spacecraft are investigated and reported. These results have been used by the Mars Global Surveyor mission planners to design the aerobraking phase of the mission. Analytical and Direct Simulation Monte Carlo computer codes were used with a detailed, three-dimensional model of the spacecraft to evaluate spacecraft aerobraking characteristics for flight in free molecular and transitional flow regimes.

The spacecraft is found to be aerodynamically stable in aerobraking and planned contingency configurations. Aerodynamic forces, moments, and heating are found to be highly dependent on atmospheric density. Accommodation coefficient is seen to strongly influence drag coefficient. Transitional flow effects are found to reduce overall solar panel heating. Attitude control thruster plumes are shown to interact with the freestream, diminishing the effectiveness of the attitude control system and even leading to thrust reversal. These plume-freestream interaction effects are found to be highly dependent on freestream density.

Acknowledgments

My educational and professional growth during my tenure at George Washington University and NASA Langley Research Center has been influenced by many people. First and foremost, I am indebted to Dr. Robert Tolson and Dr. Didier Rault. By example and instruction, they have showed me what it means to be an engineer and scientist, giving me knowledge and experience which I consider to be invaluable. In addition, their guidance, suggestions, and support have been instrumental in my research.

I would also like to thank the Aerothermodynamics Branch for creating such an enjoyable work environment. Particular thanks go to Brian Hollis, Chris Glass, and Stephen Alter for their generous assistance with computer resources. I am also grateful to Richard Wilmoth, Jim Moss, and Daniel Lyons for many stimulating and helpful discussions about DSMC and MGS. A special thanks is extended to Charles Miller for being very supportive during my stay in the Branch.

Furthermore, this work could not have been completed without the support of my family and friends.

Table of Contents

Abstract.....	ii
Acknowledgments.....	iii
Table of Contents.....	iv
List of Symbols.....	v
List of Tables.....	vi
List of Figures.....	vii
1. Introduction.....	1
2. Mars Global Surveyor Mission and Spacecraft.....	3
3. Aerobraking Maneuver and Configurations.....	5
3.1 Aerobraking Maneuver.....	5
3.2 Spacecraft Configurations.....	7
4. Flow Regimes and Solution Methods.....	9
4.1 Classification of Regimes and Kinetic Theory.....	9
4.2 Free Molecular Flow Solution Methods.....	12
4.3 Transitional Flow Solution Methods.....	14
5. Aerobraking Configuration Results.....	17
5.1 Aerodynamics.....	18
5.2 Aerodynamic Heating.....	23
6. Safing Configuration Results.....	29
6.1 Aerodynamics.....	29
6.2 Aerodynamic Heating.....	30
7. Freestream Gas - Thruster Plume Interaction.....	31
7.1 Aerobraking Configuration.....	31
7.2 Safing Configuration.....	34
8. Conclusions.....	36
References.....	38
Appendix A. Computational Tools.....	79
Appendix B. Simulation of Gas Characteristics.....	92

List of Symbols

D	drag force
L	lift force
M	moment
p	pressure
τ	shear stress
q	rate of energy transfer
V_∞	freestream velocity
ρ_∞	freestream density
A	local area
A_{ref}	reference area
L_{ref}	reference length
C_D	drag coefficient, $C_D = D / (0.5\rho_\infty V_\infty^2 A_{ref})$
C_L	lift coefficient, $C_L = L / (0.5\rho_\infty V_\infty^2 A_{ref})$
C_d	flat plate drag coefficient
C_M	moment coefficient, $C_M = M / (0.5\rho_\infty V_\infty^2 A_{ref} L_{ref})$
C_H	local heat transfer coefficient, $C_H = q / (0.5\rho_\infty V_\infty^3 A)$
C_p	pressure coefficient, $C_p = p / (0.5\rho_\infty V_\infty^2)$
C_s	shear coefficient, $C_s = \tau / (0.5\rho_\infty V_\infty^2)$
m	molecular mass
T_∞	freestream gas temperature
T_w	spacecraft surface temperature
S	speed ratio
k	Boltzmann constant
σ	energy accommodation coefficient
σ_n	normal momentum accommodation coefficient
σ_t	tangential momentum accommodation coefficient
η	normal component of momentum
ϕ	tangential component of momentum
ϵ_x	direction cosine of flow with respect to surface element X axis
ϵ_y	direction cosine of flow with respect to surface element Y axis
N	molecular number density
λ	mean free path
Kn	Knudsen number
α	freestream incidence angle
θ	freestream incidence angle

List of Tables

Table 5.1	Force coefficients for aerobraking configuration.....	48
Table 5.2	Moment coefficients for aerobraking configuration.....	48
Table 7.1	Drag, lift, and moments for aerobraking with thruster firing.....	74

List of Figures

Figure 2.1	Mars Global Surveyor spacecraft.....	39
Figure 3.1	Original aerobraking scenario.....	40
Figure 3.2	MGS aerobraking configurations, original and revised.....	41
Figure 3.3	MGS safing configuration.....	41
Figure 3.4	MGS revised safing configuration.....	42
Figure 4.1	Flow regimes for aerobraking maneuvers.....	42
Figure 4.2	Flat plate drag coefficient for various speed ratios.....	43
Figure 4.3	Flat plate drag coefficient for various temperatures.....	43
Figure 4.4	Flat plate drag coefficient for various accommodation coefficients.....	44
Figure 5.1	Freestream angle of incidence reference system, aerobraking configuration.	45
Figure 5.2	Density contours for free molecular flow field.....	46
Figure 5.3	Density contours for transitional flow field.....	47
Figure 5.4	Drag and lift coefficients vs. yaw angle, aerobraking configuration.....	49
Figure 5.5	Drag and lift coefficients vs. pitch angle, aerobraking configuration.....	49
Figure 5.6	Moment coefficients vs. yaw angle, aerobraking configuration.....	50
Figure 5.7	Moment coefficients vs. pitch angle, aerobraking configuration.....	50
Figure 5.8	Free molecular moment coefficients vs. yaw angle, revised aerobraking.....	51
Figure 5.9	Drag coefficient as function of density for various models.....	51
Figure 5.10	Drag coefficient normalized by baseline area for various deflections.....	52
Figure 5.11	Drag coefficient normalized by respective areas for various deflections.....	52
Figure 5.12	Moment coefficients for various panel accommodation coefficients.....	53
Figure 5.13	Moment coefficients for various panel accommodation coefficients, detail..	53
Figure 5.14	Pressure, shear, and heat transfer contours for free molecular flow.....	54
Figure 5.15	Heat transfer coefficient contours for transitional flow; $\alpha = \pm 15^\circ$	55
Figure 5.16	Heat transfer coefficient contours, $\alpha = \pm 30^\circ$	56
Figure 5.17	Heat transfer coefficient contours, $\alpha = \pm 15^\circ$, $\theta = 90^\circ$	57
Figure 5.18	Heat transfer coefficient contours, $\alpha = -30^\circ$, $\theta = 90^\circ$	58
Figure 5.19	Heat transfer coefficient contours for revised aerobraking configuration.....	59
Figure 5.20	Heat transfer coefficient contour lines for revised aerobraking configuration.....	60
Figure 5.21	Mean free path above sun sensor.....	60
Figure 5.22	Velocity magnitude above sun sensor.....	61
Figure 5.23	Mean free path above power shunt.....	61

Figure 5.24	Velocity magnitude above power shunt.....	62
Figure 5.25	Heat transfer coefficient along panel diagonal for various densities.....	62
Figure 5.26	Location of inboard and outboard panel diagonals.....	63
Figure 5.27	Heat transfer coefficient along panel diagonals, $\rho = 120 \text{ kg/km}^3$	63
Figure 5.28	Heat transfer coefficient along panel diagonals, $\rho = 60 \text{ kg/km}^3$	64
Figure 5.29	Heat transfer coefficient along panel diagonals; -Y panel along -Y axis.....	64
Figure 5.30	Heat transfer coefficient contours, 0° and 30° panel sweeps.....	65
Figure 5.31	Heat transfer coefficient along -Y inboard diagonal.....	66
Figure 5.32	Heat transfer coefficient along -Y outboard diagonal.....	66
Figure 5.33	Heat transfer coefficient along +Y inboard diagonal.....	67
Figure 5.34	Heat transfer coefficient along +Y outboard diagonal.....	67
Figure 6.1	Freestream incidence angle reference system for safing configurations.....	68
Figure 6.2	Moment coefficients for pitch angle; safing configuration.....	68
Figure 6.3	Heat transfer coefficient contours; revised safing configuration.....	69
Figure 6.4	Heat transfer coefficient along inner panel diagonal, revised safing configuration.....	70
Figure 6.5	Heat transfer coefficient along outer panel diagonal, revised safing configuration.....	70
Figure 7.1	Location of simulated thruster plume; aerobraking configuration.....	71
Figure 7.2	Density contour plot of aerobraking configuration with thruster firing.....	72
Figure 7.3	Pressure, shear, and heat transfer contours of aerobraking configuration with thruster firing.....	73
Figure 7.4	Yaw moment variation with density, aerobraking with thruster firing at $\alpha = 0^\circ$	74
Figure 7.5	Yaw moment coefficient, aerobraking with thruster firing.....	75
Figure 7.6	Location of simulated thruster plumes, safing configuration.....	75
Figure 7.7	Pressure coefficient contours of safing configuration with thruster firing....	76
Figure 7.8	Heat transfer contours for safing configuration with thruster firing.....	77
Figure 7.9	Pitching moment coefficient; safing configuration with thruster firing.....	78
Figure A.1	Inner and outer computational domains with spacecraft model.....	86
Figure A.2a	Normalized number of simulated molecules before steady state.....	87
Figure A.2b	Normalized number of simulated molecules at steady state.....	87
Figure A.3a	Drag coefficient before steady state.....	88
Figure A.3b	Drag coefficient at steady state.....	88
Figure A.4a	Lift coefficient before steady state.....	89
Figure A.4b	Lift coefficient at steady state.....	89

Figure A.5a	Lift to drag ratio before steady state.....	90
Figure A.5b	Lift to drag ratio at steady state.....	90
Figure A.6a	Surface collision sampling before steady state.....	91
Figure A.6b	Surface collision sampling at steady state.....	91

(

(

(

1 INTRODUCTION

The Mars Global Surveyor Program has been initiated by NASA with the goal of characterizing the planet Mars' atmosphere, gravity field, and surface properties. Every two years, a pair of spacecraft will be launched towards Mars. Each pair is to consist of an orbiter and a lander. The first orbiter, Mars Global Surveyor (MGS), was successfully launched on November 7, 1996. MGS arrived at Mars on September 11, 1997, and was captured into an elliptical orbit using conventional chemical propulsion.

"Aerobraking" in the upper atmosphere is presently being used to reduce the spacecraft orbital energy and circularize the orbit prior to the onset of scientific measurements. The research presented in this report is intended to ascertain the aerothermodynamic characteristics of MGS during aerobraking and to study the effectiveness of the Attitude Control System (ACS).

The goals of the mission and the spacecraft designed to carry them out will first be discussed. The spacecraft was designed to perform a number of scientific experiments yet be rugged enough to perform an aerobraking maneuver. A discussion of the history of aerobraking and its role in the mission will follow. This discussion will also include a description of the various spacecraft configurations employed for flight through the Martian atmosphere.

Aerobraking in the atmosphere is performed at altitudes where the flow is in the free molecule and transition regimes. Since conventional numerical methods based on the Navier-Stokes equations cannot be applied to these flow regimes, other methods must be used. The characteristics of these flow regimes will be presented, along with the methods used to obtain aerodynamic coefficients.

Results using analytical and statistical methods will be presented for various spacecraft configurations for freestream densities above and below the nominal value of 60 kg/km^3 . The aerodynamic forces, moments, and heating of the aerobraking and

contingency configurations are discussed. Finally, the effectiveness of the attitude control system for flight through the transitional regime is investigated. The interaction between the gas plume of an attitude control thruster and the freestream flow is analyzed for both configurations.

2 MARS GLOBAL SURVEYOR MISSION AND SPACECRAFT

Mission

The basic goals of the Mars Global Surveyor Mission are to:

- 1) Characterize the surface morphology at high spatial resolution,
- 2) Determine the global elemental, thermophysical, and mineralogical character of the surface material,
- 3) Define the global topographical and gravitational fields,
- 4) Establish the nature of the magnetic field,
- 5) Monitor the global weather and thermal structure of the atmosphere to evaluate the seasonal impact of the weather and thermal structure on the polar caps, atmospheric dust, and clouds.

These goals are to be achieved with a scientific payload consisting of six instruments. The instrument payload consists of a magnetometer and electron reflectometer, camera, laser altimeter, relay radio system, thermal emission spectrometer, and ultra stable oscillator for radio science. Data will be taken with the spacecraft in a low-altitude, near-polar, sun-synchronous mapping orbit over a period of two Martian years. This mapping orbit will be acquired through the use of an aerobraking maneuver¹. This type of maneuver uses atmospheric friction to create drag and reduce orbital energy until the desired orbit is achieved.

Spacecraft

The Mars Global Surveyor Spacecraft was built by Lockheed Martin Astronautics and consists of four subassemblies: the equipment module, propulsion module, solar arrays, and communication antennas. The spacecraft is shown in Figure 2.1.

The equipment module houses the avionics and science instruments and measures 1.22 x 1.22 x 0.76 meters. All of the instruments except the magnetometer are attached to the nadir equipment deck on the +Z side.

The propulsion module on the -Z side contains the main engine, attitude control thrusters, and propellant tanks. It consists of a rectangular shaped box 1.06 m on a side, not including the thermal blankets. There are three thrusters per corner; two aft facing (in -Z direction), and one for roll control (oriented normal to the others). Each thruster burns hydrazine in a mono-propellant, pulse mode.

The two solar arrays, which provide power for the spacecraft, measure 3.53 m in length and 1.85 m in width. Each array consists of an inner and outer panel which are comprised of gallium arsenide and silicon cells, respectively. "Drag flaps" made of kapton are mounted on the ends of both arrays and measure 0.81 m in length. The flaps serve to decrease the spacecraft's ballistic coefficient during aerobraking¹.

The structure which supports the solar array and connects it to the equipment and propulsion modules via electrically powered gimbals is herein referred to as the *yoke*. The orientation of the solar array assembly can be adjusted by activating the inner and outer gimbals. In an uncoupled mode, these gimbals provide rotation about the X or Y axes. If coupled, they allow the panel assembly to achieve a large number of orientations with respect to the main body.

The primary communication antenna is the 1.5 meter high gain antenna (HGA). During aerobraking, the HGA remains stowed against the equipment module and its protective cover remains attached.

3. AEROBRAKING MANEUVER AND CONFIGURATIONS

3.1 Aerobraking Maneuver

Aerobraking refers to changing the size of an orbit by using the upper atmosphere of a planet or planetary satellite to create drag. Aerobraking differs from *aerocapture* in that the latter usually involves using the atmosphere to capture an object from a hyperbolic flyby trajectory into an elliptical orbit or immediate landing. Aerocapture is quick and most of the total desired drag is obtained during a single pass through the atmosphere. Aerobraking, however, usually takes place over a longer period and the total drag is achieved gradually over a very large number of passes through the upper atmosphere.

Aerobraking has been applied in a previous planetary mission only once; specifically, it was used during the Magellan mission to Venus. After the primary mission goals were achieved, the Magellan spacecraft was aerobraked to circularize the orbit. Further aerobraking was performed during the Windmill and Termination Experiments, in which the spacecraft made multiple passes through Venus' upper atmosphere at altitudes ranging from 140 - 170 km. These experiments provided an opportunity to study the structure and behavior of the Venusian upper atmosphere. They also allowed the study of the aerodynamics of a spacecraft in a planetary upper atmosphere consisting mainly of carbon dioxide^{2,3,4,5,6}.

The use of aerobraking in the Mars Global Surveyor mission marks the first time that such a maneuver has been considered in a critical part of a planetary mission. The maneuver must be successful for the primary mission goals to be realized. Aerobraking will gradually alter the spacecraft orbit from the highly elliptical capture orbit to a nearly circular orbit needed for scientific measurements.

Aerobraking occurs near the orbit periapsis. Drag induced by aerobraking reduces the spacecraft velocity and thus energy. The reduction of energy at periapsis decreases the

apoapsis altitude. After several months, the apoapsis is decreased to the required altitude and the periapsis is then increased to terminate the aerobraking maneuver.

In the case of MGS, the aerobraking maneuver will progressively lower the spacecraft from its capture orbit (56,600 km altitude apoapsis, 353 km altitude periapsis) down to a nearly circular orbit (450 km altitude apoapsis, 350 km periapsis). The original plan was for this maneuver to be accomplished in the three phases shown in Figure 3.1

The first phase, which lasted eleven orbits, lowered the periapsis to 110 km using propulsive impulses at apoapsis with the attitude control thrusters. This gradual “walk-in” was necessitated by the large uncertainty in the atmospheric density model and allowed time to study the altitudinal and temporal variability of the atmosphere.

The second or main phase was to follow and last about three months. MGS was to make 300-400 successive passes through the atmosphere at 110 km, bringing the apoapsis down to 2000 km.

The last phase, or endgame, was to take about three weeks. During this time, the apoapsis altitude would be lowered to its final value of 450 km, and periapsis gradually raised to 143 km. Aerobraking would end with a termination burn to raise the periapsis to its final altitude of 350 km.

The plan was altered shortly into the main phase when the flight dynamic pressure, coupled with the structural condition of the panel (discussed in next section), caused panel deflections and vibrations that greatly reduced the panel’s structural integrity. Mission engineers decided that the dynamic pressure at the planned altitude of 110 km would not be safe and that the main aerobraking phase would have to take place at an altitude of about 120 km or greater, depending on the altitudinal variation of dynamic pressure. A higher altitude means less drag for each pass through the atmosphere. Thus, the new plan adds about eight months of additional time to the aerobraking maneuver to reach the final mapping orbit. The aerodynamic forces during aerobraking are expected to account for an equivalent ΔV decrease of 1300 m/s¹.

3.2 Spacecraft Configurations

The solar panels are the main drag producing structures of the spacecraft. As such, their orientation is the most significant factor in determining the amount of drag on the spacecraft and its stability characteristics.

The originally planned aerobraking configuration for MGS is shown in Figure 3.2. The solar panels are swept 30° relative to the Y axis, and the solar cells lie on the side of the panels that are not directly exposed to the freestream flow.

After launch and insertion into an interplanetary trajectory, it was discovered that the -Y solar array had not fully deployed and locked into place. The array, from the inner panel out, remained about 20.5° from full extension to the plane of the yoke. It was suspected that a shaft in the deployment damper mechanism broke shortly after launch, thereby causing the damper arm to wedge into the hinge joint between the inner panel and yoke. Recent analysis by mission engineers has determined that a second incidence of structural failure may have occurred at the yoke-gimbal interface.

Concerned that the hinge would not be able to withstand the aerodynamic torques associated with the aerobraking maneuver, MGS engineers revised the aerobraking configuration. The new configuration, hereafter referred to as the *revised aerobraking* configuration, is shown in Figure 3.2.

To obtain the revised configuration, the -Y panel assembly is first rotated 180° about the -Y axis, and the yoke is then oriented 51° from the -Y axis instead of 30° . This retains the 30° panel sweep while ensuring that any deflection of the array would be into the secured position, with the wedged damper arm doubling as a mechanical “stop”. The -Y panel solar cells are now exposed to the freestream; aerodynamic and heating issues related to this configuration are addressed in this report.

In the event of contingencies, the MGS spacecraft can adopt a “safing” configuration. This configuration will cause the spacecraft to roll over until the solar arrays

are aligned in the direction of the sun. This allows the navigation team to be fairly certain of the MGS attitude at the end of a drag pass.

To achieve this orientation from the aerobraking configuration, the spacecraft inner gimbals are rotated 65° about the Y axis toward the HGA. This configuration can be seen in Figure 3.3. There is a *revised safing* configuration associated with the revised aerobraking configuration; in this case, the panels are rotated 65° away from the HGA, as shown in Figure 3.4.

4 FLOW REGIMES AND SOLUTION METHODS

Aerobraking of the spacecraft will be conducted throughout a region of the atmosphere where the gas is highly rarefied. This region contains the free molecule and transition flow regimes. A discussion of these flow regimes and the methods of analysis for each follow.

4.1 Classification of Regimes and Kinetic Theory

Two gas molecules will collide if their trajectories are such that the distance between the centers of the molecule decreases to the molecular diameter d . The molecular *mean free path* is defined as the average distance traveled by a molecule between collisions with other molecules. It is inversely proportional to molecular number density (molecules/m³). For a gas in equilibrium with molecules that are treated as hard spheres, the mean free path λ can be determined from,

$$\lambda = \frac{1}{\sqrt{2}\pi d^2 N} \quad (1)$$

where d is the molecular diameter and N is the local number density of the mixture⁷.

Classification of Regimes

The mean free path is an important parameter in determining the type of flow regime. The parameter often used to classify the regimes is the *Knudsen* number,

$$Kn = \frac{\lambda}{L} \quad (2)$$

where L is some characteristic reference length. *Free molecular* flow is usually considered to exist for $Kn > 10$, and *transitional* flow for Kn in the range 0.1 - 10.0. In both regimes, the molecules will give up a fraction of their energy and momentum upon collision with a surface. The differences between regimes arise when molecular behavior before and after surface collisions is analyzed.

In free molecule flow, the molecules are not considered to significantly interact with the freestream after reflection with a surface. Or, conversely, a freestream molecule can be expected to travel the distance from upstream of the spacecraft to the spacecraft surface without encountering another molecule. Likewise, the molecule will only impact the spacecraft once.

Transitional flow occurs when intermolecular collisions become significant and cannot be ignored. As these collisions increase in number and significance, the flow approaches the continuum regime.

A more accurate determination of Kn is obtained by using the *local* mean free path, evaluated in the flow field near the spacecraft instead of in the freestream, since any significant collisions between molecules would take place between the reflected (or local) molecules and freestream molecules.⁷

Figure 4.1 shows the trajectories of the Magellan and MGS spacecraft in a Mach-Reynolds-Knudsen number plot. Aerobraking at Mars will take place in the Mach 20-30 range over the atmospheric density spectrum. In the course of an aerobraking pass, the spacecraft passes from the free molecular regime at high altitudes to deep into the transition regime around periapsis, and then back out into the free molecular regime. It can be seen that at the nominal periapsis density, Kn is about 0.2, which is well into the transition flow regime. In contrast, aerobraking in the Magellan mission was performed at higher Knudsen numbers, where the free molecular regime dominates.

Once the type of regime that is being encountered is determined, the evaluation of spacecraft aerodynamic properties in the regime must be performed.

Kinetic Theory

The *velocity distribution function* provides a statistical description of a gas at the molecular level. Macroscopic gas properties can be computed by obtaining *moments* of the distribution function. For example, the *0th* moment would give gas density, the *1st* moment provides velocity, and the *2nd* moment yields temperature⁷.

A gas in equilibrium has a Maxwellian velocity distribution function which is exponential in form. For a polyatomic gas, a separate distribution function is needed for each species in the gas. The pertinent equation in the rarefied flow regime is the *Boltzmann* equation, which is an integro-differential equation whose solution in principle would yield the velocity distribution function for each gas constituent.

Any rarefied gas dynamics analysis must be obtained by simplifying or solving the Boltzmann equation in some manner⁸. The Chapman-Enskog method provides a solution of the Boltzmann equation for a restricted set of problems in which the distribution function is perturbed by a small amount from the equilibrium Maxwellian form. Derivation of this method provides expressions for viscous stress and heat flux that can be substituted into conservation equations to obtain the monatomic gas form of the Navier-Stokes equations. However, these are obtained assuming a *small* perturbation from equilibrium, which would imply a restriction on the size of flow gradients. Thus, the Navier-Stokes equations cannot be applied to most rarefied gas problems⁸.

The method of obtaining a solution to the Boltzmann equation depends on the particular situation. For free molecular flow, intermolecular collisions by definition are not significant and thus collision terms may be eliminated from the Boltzmann equation. This greatly simplifies the situation and enables an analytical, closed form solution to be obtained⁸.

4.2 Free Molecular Flow Solution Methods

Analytical equations for free molecular flow are derived by disregarding collisions and assuming an equilibrium velocity distribution. The resulting equations are functions of the velocity and temperature of the freestream, the temperature of the spacecraft, and material properties modeled as *accommodation coefficients*.

The energy accommodation coefficient σ is an important parameter used to characterize the amount of energy given up by a molecule to a surface upon collision. This parameter is defined by,

$$\sigma = \frac{q_i - q_r}{q_i - q_w} \quad (3)$$

where q_i and q_r represent the incident and reflected energy fluxes, respectively⁷. The variable q_w is the energy flux that pertains to reflection with surface (wall) temperature T_w . *Diffuse* reflection corresponds to complete thermal accommodation where all molecular energy is given up to the surface. In this case, $q_r = q_w$ and $\sigma = 1$. *Specular* reflection corresponds to a perfectly elastic collision, where $q_r = q_i$ and thus $\sigma = 0$. An analogous *momentum* accommodation coefficient is also defined, and is usually decomposed into normal and tangential components.

The normal momentum accommodation coefficient is defined as,

$$\sigma_n = \frac{\eta_i - \eta_r}{\eta_i - \eta_w} \quad (4)$$

where η is the normal component of momentum. The tangential coefficient is determined from,

$$\sigma_t = \frac{\varphi_i - \varphi_r}{\varphi_i - \varphi_w} \quad (5)$$

with tangential momentum component ϕ . For diffuse reflection, all momentum is transferred to the surface. However, for specular reflection, the normal component of momentum is reversed while the tangential part remains unchanged.

Another variable in the free molecular equations is the speed ratio, which replaces the Mach number in rarefied flow regimes. This parameter is defined as the ratio of the freestream, or spacecraft, velocity to the mean molecular velocity. For aerobraking at Mars or Venus, the free molecular equations show a greater dependence on accommodation coefficient than on speed ratio or spacecraft surface temperature.

Figure 4.2 contains a plot of flat plate drag coefficient vs. incidence angle for free molecular flow at two different speed ratios. Drag coefficient has been normalized by the flat plate projected area which varies with incidence angle. For MGS, the speed ratio at walk-in was about 20 and is 14 for the original endgame. Note that the value in C_d at 90° incidence increases by only 3% for a 30% decrease in speed ratio from 20 to 14. Thus, changes in spacecraft velocity will not have a large effect on drag coefficient.

Figure 4.3 shows the variation of drag coefficient with wall and freestream temperatures T_w and T_∞ , respectively. At most, C_d only changes 1.4% for a 50% increase in T_w . This allows considerable uncertainty in spacecraft temperature without a loss of accuracy in predicting drag coefficient. Also note that for a given T_w , variation in T_∞ has little effect on drag coefficient. Thus, a precise knowledge of freestream temperature is also not essential in determining C_d .

The variation of drag coefficient with normal and tangential momentum accommodation coefficients is shown in Figure 4.4. C_d decreases by as much as 10% when the normal coefficient is decreased from 1.0 to 0.9. This significant change arises because a lower σ_n means less diffuse reflection; the closer to specular reflection, the greater the momentum that is imparted to a surface. Consequently, a 10% uncertainty in accommodation coefficient can lead to drag predictions that are in error by the same amount.

Thus, the assumption of an accommodation coefficient is very important in evaluating the aerodynamics of a spacecraft in free molecular and transitional flow. In the Magellan Windmill Experiment, accommodation coefficient was found to vary with freestream incidence angle^{3,4}. In the Termination Experiment, it was difficult to ascertain the accommodation coefficient of the spacecraft because of exhaust plumes, dependence on incidence angle, and other factors. The only conclusion that could be made was that the value lay somewhere between 0.8 and 1.0^{2,3}.

With this in mind, most of the analyses performed in this report assumed energy and momentum accommodation coefficients of 1.0. This would be considered to be a very conservative value, since it allows the spacecraft to receive the greatest amount of heating and the lowest amount of drag.

4.3 Transitional Flow Solution Methods

The significance of intermolecular collisions in transitional flow prevent the simplification of the Boltzmann equation by elimination of collision terms. This leaves the full equation to be solved. The lack of a closed form, analytical solution necessitates the use of numerical methods. There are numerical methods available to solve the integro-differential equation for the velocity distribution function itself, yet direct simulation solutions are more readily obtained⁸. Direct simulation solutions do not solve the Boltzmann equation but rather model the physics of the gas flow. This involves the tracking of a representative sample of molecules throughout a time period in which molecules collide with each other and perhaps with a surface.

Direct Simulation Monte Carlo differs from earlier simulation methods in the manner that collisions are handled. In other methods, an initial configuration of molecules is set, and the collisions are deterministic. That is, the trajectories of molecules are computed and intermolecular collisions occur when two trajectories converge to the

molecular diameter. For each trajectory, all other molecules are examined as possible collision partners. In DSMC, however, the collision computations are *probabilistic*⁸. DSMC has been found to be less computationally intensive than the earlier methods and can be applied to a larger number of flow situations. In order to discuss the method in which collisions take place, it is first necessary to discuss the simulation region.

The simulated region in DSMC is sub-divided into cells. Cells are needed to define the geometry of the body in question, identify molecular collision partners, and sample macroscopic quantities used to generate a solution. The cells must have dimensions such that the change in flow properties across each cell is small. Time is advanced in increments that should be small in comparison with the mean collision time per molecule. Yet, strict adherence to these requirements are not necessary and deviations from them do not create significant variations in results. Simulation parameters such as cell size, time step, and number of molecules are dependent on the particular application. For example, for a simulation of a strong shock wave, the cell size and time step are not critical so long as there are at least twenty molecules per cell and the ratio of cell size to time step is not several times the speed of the shock⁶. In addition, grid resolution studies showed that in the case of a boundary layer, coarse grids do not restrict flow gradients and these solutions accurately match a fine-grid solution⁹.

The DSMC approach is related to the Boltzmann equation by the restriction to binary collisions in every cell and the treatment of these collisions as instantaneous events. For a discrete time step, the molecular motion and collision terms of the Boltzmann equation are decoupled. This allows the simulated gas particle to be considered in terms of two consecutive but distinct events in one time step. Specifically, there is a collisionless motion of all the particles (which is deterministic) followed by a motionless collision of those pairs of particles which have been identified as collision partners (through probabilistic means).

In essence, a single time step consists of:

- 1) Collisionless motion of particles.
- 2) Enforcement of boundary conditions.
- 3) Pairing of collision partners.
- 4) Collision of selected collision partners.
- 5) Possible sampling for macroscopic flow quantities, depending on sampling frequency.

There are many models that attempt to simulate actual collision characteristics. A popular model is the *variable hard sphere* (VHS) molecular model. In this model, the molecular diameter d is a function of the relative velocities of the molecules. In addition, uniform, isotropic scattering is permitted. The *collision cross section*, which is proportional to the square of d , is a function of the molecular velocities.

Collision partners are paired using a probability function. The probability of a collision between two molecules in a gas is proportional to the product of their relative velocities and total collision cross section. A molecule is then determined to be a collision partner by application of the *acceptance-rejection* method.

Using a set of randomly generated numbers, every collision pair in a cell is assigned a number. The collision probability is then compared to this random number. If the probability is greater than the number, the collision pair is accepted. If the probability is less, the molecules will not collide⁸. A method that is often used in conjunction with the acceptance-rejection method is to limit the number of molecules that are allowed to be considered for collisions. This is done by randomly selecting a number of molecules in each cell.

The VHS model, decoupling of molecular motion and collisions, and the acceptance-rejection method are implemented in the LaRC 3D DSMC algorithm¹⁰.

5. AEROBRAKING CONFIGURATION RESULTS

The aerodynamics of Mars Global Surveyor were investigated earlier during the design phase of the mission¹¹. The results in this report reflect the aerothermodynamic characteristics of the actual flight spacecraft. Even though the earlier results were obtained using a simpler computational model, the overall aerodynamic trends have been validated and are discussed herein.

Results will be presented for free molecular flow, and for transitional flow corresponding to freestream densities ranging from 1/20 of the nominal density of 60 kg/km³ to twice the nominal value. Freestream characteristics are given in the Appendix. Unless otherwise noted, a value of 1.0 was used for momentum and energy accommodation coefficients.

The reference system for freestream angle of incidence is shown in Figure 5.1. The freestream velocity vector relative to body-fixed axes is related by:

$$V_x = -V \sin\alpha \sin\theta$$

$$V_y = V \sin\alpha \cos\theta$$

$$V_z = V \cos\alpha$$

Flow Field

The aerodynamics of the spacecraft are directly influenced by the flow field around the spacecraft. As discussed earlier, aerobraking takes place in the free molecular and transitional flow regimes. These regimes will cause the flow field around the spacecraft to change as the spacecraft penetrates deeper into the atmosphere. This variation is exhibited in Figures 5.2 and 5.3 using results obtained with DSMC for freestream flow along the Z axis.

Figure 5.2 shows a normalized number density contour plot of carbon dioxide in the free molecular regime. The flow field around the spacecraft can be seen to take the

form of a relatively large and diffuse gas layer. This flow structure was achieved by running the DSMC code in collisionless mode. This mode does not allow inter-molecular collisions but differs from free molecular analytical code in that the molecules have a *thermal velocity* component associated with their motion. The thermal velocity is the velocity of a molecule relative to the freestream velocity and can be viewed as being a random velocity. The contribution of this velocity component is the reason why there are no sharp flow field boundaries in regions behind spacecraft gaps or edges, such as at the end of the drag flap.

As the flow regime progresses to transitional, the gas layer becomes smaller. Figure 5.3 is a density contour plot for flight at a density of 60 kg/km^3 . The flow field has now taken the form of a thin shock layer. This layer influences the aerodynamic forces, moments, and heating on the spacecraft.

5.1. Aerodynamics

During normal aerobraking, the spacecraft attitude may deviate from zero angle of attack by as much as 20° . This situation necessitated the evaluation of spacecraft aerodynamics for a range of angles.

Drag, Lift, and Moments

Values of force and moment coefficients for the original configuration for various freestream flow angles at a density of 120 kg/km^3 can be found in Tables 1 and 2. Reference area and length are also given. Reference area corresponds to the projected frontal surface area of the computational model; reference length is usually taken as the distance from the tip of one solar panel to the other.

Drag and lift coefficients are plotted vs. yaw and pitch angles in Figures 5.4 and 5.5, respectively. *Yaw* is defined here to refer to flow confined to the Y-Z plane ($\theta = 0^\circ$),

and *pitch* refers to flow restricted to the X-Z plane ($\theta = 90^\circ$). Figure 5.4 shows that, as expected, drag is greatest at zero incidence, and only changes by about 10% out to a 30° change in α . Inspection of Figure 5.5 reveals a similar variation with even less difference between C_D values at $\alpha = 0^\circ$ and 15° . This is because the high gain antenna makes up for most of the drag that is lost with non-zero incidence. The contribution to drag by the HGA should not be discounted if alternate flight configurations are to be considered in the event of equipment malfunction. Also note the insignificance of lift coefficient in comparison to drag; this is inherent to the spacecraft design and planned flight attitudes.

Transitional flow effects reduce drag by about 11%. Drag is reduced because the shock layer that develops upstream of the spacecraft partially shields it by scattering incoming freestream molecules. This results in lower pressure and shear on the spacecraft. The decrease in drag due to transitional effects and variation in attitude is not large when considering an individual drag pass. However, the 10-11% reduction is indeed significant when added over the time of the whole maneuver.

Yaw and pitching moments are plotted as functions of angle of incidence up to 30° for free molecular flow in Figures 5.6 and 5.7. Transitional flow results are included for selected angles as well. The stability of MGS (null moment at 0° and negative slope for C_{My} and C_{Mx} vs. α) is exhibited in these figures, and the curves validate earlier results¹¹. It can be seen that there is little difference between free molecule and transitional values for yaw moment; however, there is a significant difference in pitching moment values which can be ascribed to asymmetries about the Y-Z plane, most notably the HGA. Transitional flow reduces the slope of the curve which implies a slight decrease in stability.

Figure 5.8 contains a free molecular moment plot for the revised aerobraking configuration to demonstrate that the stability characteristics of the original configuration are maintained.

Variation with Freestream Density

The variation of drag coefficient with freestream density was investigated for the revised aerobraking configuration. Drag coefficients were obtained for density cases of $\rho = 150, 120, 60, 12,$ and 3 kg/km^3 . The freestream velocity magnitude was kept fixed at 4811 m/s and angles $\alpha = \theta = 0^\circ$.

These values are plotted in Figure 5.9. Results from an earlier model which did not contain drag flaps are included in this figure. The trends of C_D vs. ρ are in very good agreement between the two models. Differences in values can be attributed to model differences, namely, the increase in reference length with the addition of drag flaps. Since Knudsen number is inversely proportional to reference length, an increase in length would lead to a smaller Knudsen number, thereby increasing transitional effects and decreasing C_D .

A functional form for C_D vs. ρ was obtained for the current results and the corresponding curve is shown in the figure. This function is:

$$C_D = 1.860 - 0.1733 * X - 2.866 * 10^{-2} * X^2, \quad X = \log_{10}[\rho / 1.2E-7] \quad (6)$$

This curve lies within 3% of all the points in the plot, and approaches the free molecular limit of 2.13 as density approaches zero. This curve is useful to mission planners and engineers in that it clearly predicts what drag coefficient to expect for a wide range of densities. It also demonstrates the non-linear variation of transitional effects with density.

Careful examination of Figure 5.9 reveals an unusual trend for both models. The value at 12 kg/km^3 lies significantly below a curve fit through all the points in each model. It appears that two curves with different slopes could be drawn; one curve for $\rho < 12 \text{ kg/km}^3$ and another one for $\rho > 12 \text{ kg/km}^3$. Comparison with results from a third model shows the same trend [Wilmoth, R., private communication]. It is uncertain whether this trend is a computational artifact due to the characteristics of the cells or an actual flow phenomenon; further study may be warranted to understand this situation.

Flexible Solar Panel

The partial deployment of the -Y solar array early in the mission eliminated the ability to treat it as rigid and lead to the examination of the aerodynamics associated with a flexible panel. During interplanetary cruise, vibration tests were performed which determined an approximate spring constant for the panel. Analysis using this spring constant gave a prediction of 10° of deflection at the maximum expected dynamic pressure. The determination of the effect such a deflection would have on spacecraft drag coefficient was investigated.

Three density cases with the panel deflected 10° about the panel - yoke "hinge" line were analyzed. This deflection gives the -Y panel an effective sweep of 40.5° . Figure 5.10 compares the drag coefficient with and without deflection of the panel. This panel deflection gives an area ratio A_{ref10} / A_{ref0} equal to 0.944, or a 6% difference. In this figure, drag is normalized by the nominal reference area for both cases. This normalization provides a non-dimensional estimation of how much drag is reduced when the panel is deflected, or, the effect of reduced projected area. The 6% difference in free molecular C_D limits is essentially due to the 6% reduction in projected area. This difference is maintained throughout the higher densities. At $\rho = 120 \text{ kg/km}^3$, there is a 9% difference in drag coefficient.

It should be noted that although the value for area tends to be an overestimation of the actual projected area, which is due to the discretization method, it is indeed a relevant area and is obtained from the same model as the aerodynamic results. To maintain consistency with the results, this area must be used.

Figure 5.11 is a plot comparing values that have been normalized by the respective reference areas for each configuration. This normalization removes projected area effects as a possible factor in differences in drag coefficient. The only relatively significant difference occurs at the highest density of 120. The coefficients differ by about 3% at this density.

For a given reference length, an increase in density will decrease the mean free path and decrease Knudsen number. A lower Knudsen number means an increase in transitional effects. Thus, this distinction in drag coefficient values might be explained by transitional effects and would account for the remaining 3% C_D difference not due to reduced area.

This analysis shows that the change in drag with panel deflection is mostly due to reduction of projected area and transitional effects are not significant. In addition to the curves just discussed, a database containing forces and moments as functions of density, attitude, and panel deflection is very useful to mission engineers for it provides a method to estimate the actual panel deflection from measured quantities.

It is important to note that for both 0° and 10° deflection cases, the freestream was aligned along the spacecraft +Z axis, which is not an equilibrium orientation for the 10° deflection. The equilibrium C_D would lie approximately halfway between the two curves, corresponding to an equilibrium angle of about 5° .

Variation of Equilibrium Angle with Accommodation Coefficient

In addition to panel deflection, accommodation coefficient strongly influences drag coefficient, as discussed earlier. The “flipping” of the -Y panel to expose the solar cell side to the freestream raised the issue of unequal accommodation coefficients between the +Y and -Y panels. The effect of this on equilibrium, or trim, angle was analyzed.

Figure 5.12 contains a plot of yaw moment coefficient vs. incidence angle for various configurations and momentum accommodation coefficients (AC) for free molecular flow. The original configuration with $AC = 1.0$ is compared to the revised configuration with values of 1.0, 0.8, and 0.6 for the -Y panel (yoke and flap accommodation coefficients kept constant at 1.0). Figure 5.13 shows a detailed view in the range of values around the equilibrium angle.

Note that the trim angle shifts almost two degrees from the original configuration to the revised while accommodation coefficient is kept fixed at 1.0. This is due to the increased sweep of the +Y panel; equilibrium shifts in the direction of reduced projected area. The trim angle then shifts almost three degrees from the new position when accommodation coefficient is decreased to 0.8. The change is almost six degrees for the extreme case of $AC = 0.6$. The value of 0.8 is not unrealistic since results from the Windmill Experiment showed normal and tangential momentum accommodation coefficients to be nearly 0.8 for a 30° panel sweep⁴.

This in itself may not appear to be significant. But, it cannot be discounted when other variables that affect trim angle, such as atmospheric winds and panel deflection, also produce $2^\circ - 5^\circ$ of change in trim angle. Contributions from wind and panel deflection were seen in data from early aerobraking passes.

5.2 Aerodynamic Heating

Heating rate calculations at a freestream density of 120 kg/km^3 were performed in the spacecraft design phase to help designers lay out solar panel thermal insulation and protective paints¹¹. Recent calculations confirm trends that were discovered during the design phase, and further investigate panel heating.

Free molecular flow gives a uniform pressure, shear, and heat transfer distribution on the panel, as seen in Figure 5.14 with the revised configuration (distribution on the yoke is different due to the greater yoke angle). These contours were obtained with DSMC in collisionless mode. For transitional flow, the heat load is higher near the panel edges and lower in the middle, as seen in the orientations displayed in Figure 5.15. This difference occurs because of the upstream shock layer that scatters incoming freestream molecules. The thickness of this layer decreases as the panel edge, or undisturbed flow boundary, is

approached. The fewer the molecules that reach the middle of the panel, the lower the amount of energy, or heat, that is transferred to the surface.

Figure 5.15 compares the nominal case ($\alpha = 0^\circ$, $\theta = 0^\circ$, flow along Z axis) with cases where the flow is at an incidence of approximately 15° in the YZ plane ($\alpha = \pm 15^\circ$, $\theta = \pm 15^\circ$). The panels that are inclined into the flow receive greater heating as expected. Figure 5.16 compares the nominal case to the $\pm 30^\circ$ ($\theta = 0^\circ$) incidence cases which show similar trends. Figures 5.17 and 5.18 contain cases for flow at $\alpha = \pm 15^\circ$ and -30° incidence, respectively, when the flow is confined to the XZ plane ($\theta = 90^\circ$). Notice the heating along the panel edges. The -30° incidence case receives slightly less heating as it is less exposed to the flow; however, the shear coefficient for this case would be greater than for the 15° . The variation of C_H with flow incidence angle allows mission engineers to determine if and where any excessive heating may occur during the mission, and to plan accordingly.

Aerodynamic Heating for Revised Aerobraking Configuration

Heating trends for the revised configuration were investigated since the solar cells on one panel are now exposed to the freestream and must not exceed temperature limits. Figure 5.19 shows heat transfer contours over the whole spacecraft for a freestream density of 120 kg/km^3 and 0° flow incidence to the spacecraft. The only significant difference from the original configuration is that the -Y yoke receives less heating than the +Y since its angle relative to the incident flow is greater. Contour lines over the -Y panel and drag flap are shown in Figure 5.20. The scattering of molecules from the center of the panel is evidenced by lower heat transfer coefficients.

Local Heating for Revised Aerobraking Configuration

The flow field characteristics about the solar panel were evaluated to determine if there would be any excessive heating on instruments mounted on the panels. These instruments included a power shunt, diode and sun sensor. The power shunt is located on the yoke; the diode and sensor are located near an edge of the inboard panel on opposing corners, with the sensor is nearest the outboard panel. The local mean free path and velocity of the flow just above the instruments were determined.

The local mean free path vs. distance from the panel centerline is shown in Figure 5.21 with the location of the sensor indicated. The dimensions of the sun sensor are about 7" long, 3" wide, and 2" high. The mean free path is about 2 cm, or 0.8 in., in the vicinity of the sensor. The magnitude of velocity, as shown in Figure 5.22, is about 150 m/s.

The mean free path above the power shunt is about 3 cm (1.2 in), and the velocity 100 m/s, as seen in Figures 5.23 and 5.24, respectively. Each section of the shunt measures approximately 12" in length, 2" in width, and 1" in height.

A comparison of mean free path to instrument width and height shows that the values of λ are on the order of the instrument size and flow velocities are subsonic (speed of sound is approximately 236 m/s). Therefore, there are no shocks directly above the instruments, and since the flow does not exhibit continuum characteristics, heat transfer associated with the continuum regime is not an issue.

Aerodynamic Heating Variation with Freestream Density

Mission engineers were interested in the variation of solar panel heating with freestream density, particularly for the revised configuration. This allowed them to know the heating characteristics of the solar arrays over a wide range of flight conditions. The variation of heat transfer coefficient across the inner and outer panels for a number of

freestream densities was calculated to assist the engineers in developing solar panel thermal models.

In Figure 5.25, heat transfer coefficient is plotted against distance along the inner panel diagonal for five freestream densities: 150, 120, 60, 12, and 3 kg/km³. The diagonal starts from either corner nearest the yoke, as shown in Figure 5.26. Each inner and outer panel measures about 73 inches in width by 60 inches in length. There is a strong variation in C_H across the panel for the higher densities. As density decreases to 3 kg/km³, there is little variation as the flow regime approaches free molecular.

In addition, transitional effects are greater for the outboard panel than the inboard. This is exhibited in Figures 5.27 and 5.28, which are plots of C_H vs. distance along a diagonal for both inboard and outboard panels at densities of 120 and 60 kg/km³, respectively. The outboard diagonal starts from the corner nearest the inboard panel, as shown in Figure 5.26. C_H drops off more rapidly with diagonal distance for the outboard panel than the inboard; the outboard has less edge heating than the inner and thus a larger region of lower heating as seen in Figure 5.19. This gives lower overall values for the outboard panel than for the inboard. By 12 kg/km³, the differences between inboard and outboard curves are insignificant as the free molecular regime is approached.

This variation of C_H between panels is due to the freestream being at some incidence angle with respect to the panel assembly. For a non-zero incidence, molecules above the inboard panel get pushed along the panel towards the outboard and create a thicker molecular layer there, thus increasing the shielding of the panel. Figure 5.29 contains a plot of C_H vs. distance along both panels for a case where the -Y panel is along the -Y axis; that is, the flow is at 0° incidence to the panel. There is little difference in center region C_H between panels. Thus, transitional effects are fairly evenly distributed.

Figure 5.30 presents this trend using C_H contours. A panel assembly at some angle, or sweep, is compared to the assembly with none (panel along Y axis). A zero sweep to non-zero sweep comparison of each panel member reveals that this angular effect

can be applied to a single flat plate, not just a collection of them. For example, inspection of the inboard panel with sweep shows that the center region of one half of the panel has greater heating than the other half. Comparing this to the no-sweep inboard panel member reveals no difference in center region heating throughout the member.

Aerodynamic Heating for Alternate Configuration

A similar analysis was performed to investigate the aerodynamic heating on the spacecraft in the case where the solar panel sweep is reduced from the nominal 30° . The objective for such a configuration is to give the ability to raise the spacecraft aerobraking altitude in the event of excessive heating. A raise in altitude would mean lower atmospheric density, and presumably lower heating. In order to maintain the same amount of drag, the panels must be oriented to create a larger projected area. This is achieved by reducing the panel sweep.

The revised aerobraking configuration, henceforth referred to as the *baseline* in this analysis, was modified such that the -Y panel was oriented along the -Y axis, and the +Y panel kept at a sweep of 33.8° relative to the Y axis. This new configuration will be referred to as the *reduced sweep* configuration. The trim angle for such a configuration is -18.4° . This gives effective sweeps of 18.4° for the -Y panel, and 15.4° for the +Y panel if the spacecraft is oriented at its trim angle.

The projected area for the reduced sweep configuration at such an attitude is estimated to be 18.15 m^2 . Comparing this to the projected area value of 17.44 m^2 for the baseline configuration at 0° incidence gives a 4% increase in area for the new orientation.

Figures 5.31 and 5.32 contain plots of C_H vs. diagonal distance along inboard and outboard panels, respectively, for the -Y panel. Values are compared to those for the baseline configuration. Figures 5.33 and 5.34 contain the same information for the +Y panel. All results were obtained at a density of 120 kg/km^3 . For the -Y panel, the largest heating difference occurs at the corners. The largest ΔC_H for the inboard is 20%, while for

the outboard it is 10%. For the +Y panel, the largest inboard ΔC_H is about 11%; for the outboard it is approximately 17%.

The reduced sweep configuration increases drag by about 17%. Thus, an increase in drag is obtained at a “cost” of roughly the same percentage of heating. Since drag and heating are both directly proportional to density, nothing is gained. To reduce heating, the altitude must be raised to where the 20% ΔC_H is eliminated, eliminating the gain in drag at the same time. In other words, flight at a higher altitude would maintain the same amount of heating and drag when reducing sweep.

However, the preceding analysis assumes a constant periapsis velocity. If the velocity is reduced, then the altitude where the increase in heating is removed is *not* the same altitude at which the gain in drag is removed. Drag is proportional to V^2 , but heating is proportional to V^3 . Thus, as the altitude is raised with a velocity reduction, the heating increase will be nullified before the drag increase. Therefore, there is some altitude at which a gain in drag can be achieved without any penalty in aerodynamic heating.

6. SAFING CONFIGURATION RESULTS

6.1 Aerodynamics

In the event of contingencies, flight software will command MGS to adopt the safing configuration. During this maneuver, the attitude control system is in a rate limiting mode and so the fuel usage will depend on the maximum moments that the control system will have to restrain. The nature of such an event precludes knowledge of the spacecraft orientation relative to the freestream at the beginning of its occurrence. The aerodynamics of MGS was therefore investigated over a wide range of orientations, but confined within the X-Z plane.

The reference system for angle of incidence for both original and revised configurations is shown in Figure 6.1. This reference system is chosen to coincide approximately with the equilibrium angle. That is, zero incidence is chosen so that regions of stability are more obvious. The components of the freestream velocity vector are determined from,

$$V_x = V \cos\alpha$$

$$V_z = V \sin\alpha$$

Pitching Moments and Stability

The moment coefficient about the Y axis C_{M_y} for the original safing configuration is plotted as a function of pitch angle in Figure 6.2. Free molecular results are presented at 15° intervals for accommodation coefficients (AC) of 1.0 and 0.8; transitional results are presented for the angles 0°, 30°, 60°, 120°, 180°, and -135°. All transitional flow results correspond to a freestream density of 120 kg/km³.

These results suggest that using the free molecular moment values with accommodation coefficient of 1.0 would provide a conservative estimate of fuel usage since

these are the greatest values. Note that transitional effects serve to decrease the moments and are most significant at -135° and 60° .

Inspection of the curve at $\alpha = 0^\circ$ suggests that the stable trim angle is a few degrees below the X-Y plane, noting that it is sensitive to assumptions about accommodation coefficient. This uncertainty in trim angle is a consideration for attitude control after safing. Also, there is an unstable equilibrium at 180° , while -60° and 120° are near-equilibrium.

Moments about X and Z are not shown because their magnitudes are no greater than 0.01 over the complete range of incidence angles α .

6.2 Aerodynamic Heating

A thermal analysis of the *revised* safing configuration was performed to determine the regions of greatest heating on the solar panel. Heat transfer coefficients for the spacecraft at the approximate trim angle of $\alpha = 7^\circ$ were obtained for a freestream density of 120 kg/km^3 .

Figure 6.3 shows C_H over the whole spacecraft. Greater heat transfer is visible around the upper portion of the panel, which is now the leading edge, while less heating arises at the lower, trailing edge. Heat transfer coefficient is plotted against distance along diagonal 2 for the inboard and outboard panels in Figures 6.4 and 6.5, respectively. Diagonal 2 begins in the upper corner near the yoke, as shown in Figure 6.3. A stronger C_H gradient exists along the inboard panel than the outboard.

A comparison with C_H trends for the aerobraking configuration show a significant difference in gradients but not in maximum heat transfer. An important distinction is that the revised safing configuration encounters less overall heating than the revised aerobraking configurations. This information was used by the mission engineers to help develop a solar panel thermal model to supplement that existing for the aerobraking configuration.

7. FREESTREAM GAS - THRUSTER PLUME INTERACTION

Thruster firings may occur during aerobraking due to planned operations, large attitude excursions, or attitude rate control. Interaction effects between the thruster gas plume and the freestream flow were first discovered during the Termination Experiment in the Magellan mission. Discrepancies between flight and predicted data for aerodynamic torques on the spacecraft were best explained by considering the effects of the interaction between plume and freestream^{2,3,11}. A thruster plume may prevent some of the incident freestream from reaching certain portions of a spacecraft. This interaction will redistribute forces on the spacecraft and induce moments.

Additional studies found significant interaction effects for the Mars Global Surveyor spacecraft¹². The interaction between the Mars Global Surveyor ACS thruster plumes and the freestream has been revisited and investigated for both aerobraking and safing configurations.

7.1 Aerobraking Configuration

A DSMC simulation for the interaction between one thruster and the freestream at 0° incidence (flow along +Z axis) was performed at a freestream density of 120 kg/km³ for the original aerobraking configuration. The jet that is fired is located at the corner nearest the -Y panel yoke and the high gain antenna as indicated in Figure 7.1. Thruster plume characteristics are given in the Appendix.

When the thruster fires, the solar panel closest to the thruster is partially shielded from the freestream; in effect, the plume creates a “shadow” on the panel. The formation of this shadow can be visualized in Figure 7.2, a contour plot of the normalized molecular number density of CO₂, the dominant species in the freestream gas mixture. In Figure 7.3,

the effect of the shadow is evident in contours of pressure, shear, and heat transfer coefficient.

The plume effect on drag and pitching moment is significant. The plume interaction will induce a 7 N, or 15%, *decrease* in total drag and a 5.8 N-m *change* in total yaw moment. Given a thruster force of 3 N, the increase in aerodynamic moment is opposite in direction to the 2.6 N-m torque induced by the thruster firing; thus, the net moment of 3.2 N-m is opposite in direction to the one intended. This result has been termed "thrust reversal". In essence, if a thruster is fired to induce a moment in one direction, the result is a torque in the opposite, non-desired direction.

Plume-freestream effects were investigated for dependence on freestream density. Results were obtained for the additional density cases of 60 and 40 kg/km³ at the zero freestream incidence angle. Table 7.1 contains yaw moment values and their non-dimensional coefficients, along with the net drag, lift, and moment contributions from the yokes and inner panels, respectively. For this plume analysis, the yoke is defined here to include the small portion of the inner panel that is left after cutting the corners to permit stowing for launch.

The table also includes moment values for the solar array only. There is an appreciable difference between the values for the panels and the total spacecraft due to the main body (equipment and propulsion modules) being partially shadowed by the plume.

The table values for yaw moment are plotted as a function of density in Figure 7.4. As expected, yaw moment can be seen to decrease with a decrease in density. A least squares fit was used to draw a curve through the three data points for the complete spacecraft to extrapolate the results to zero density, where it is known that the moment must be zero.

Since the yaw moment is positive, and the torque produced by the jet is negative, the effect of the plume at low densities is to diminish the effectiveness of the thruster. As the density is increased, there is more plume-freestream interaction and therefore more

shadowing. At $\rho = 28 \text{ kg/km}^3$, the total spacecraft pitching moment is equal to the jet torque. Beyond this density, the aerodynamic moment is greater and thrust reversal occurs.

It should be noted that the pitching moment C_{My} is included in the table but its value is an order of magnitude smaller than the yaw moment and its variation with density is insignificant.

Since the thrusters will be used to control angular rates in addition to correcting attitude deviations from equilibrium or other angles, it was necessary to investigate plume-freestream interaction effects for non-zero angles of incidence.

Figure 7.5 shows yaw moment coefficient as a function of angle of incidence for cases with and without a jet. The freestream density is 120 kg/km^3 . The reference system is the same as that in Figure 15 as is the jet that is fired. Transitional flow results were obtained at angles of $\alpha = 0^\circ, \pm 7^\circ$, and $\pm 15^\circ$ and $\theta = 0^\circ$. These results can be analyzed for three different mission situations.

First, if the spacecraft is at $\alpha = 0^\circ$ and a non-zero attitude angle is desired, the thrusters would have to be fired to create the necessary torque. However, given the previous discussion, thrust reversal will occur if such an action takes place. A method of avoiding this would be to acquire the desired attitude before the spacecraft encounters atmospheric densities above 30 kg/km^3 , or even before atmospheric entry.

The second scenario that employs the use of thrusters is if a correction to a non-zero attitude must be made and the natural restoring moment is not sufficient to return to the equilibrium angle of 0° . The thruster chosen for simulation will fire for positive angles of incidence. This would add negative torque to the negative aerodynamic moment. As seen in Figure 7.5, the plume-freestream interaction causes no significant change to the moment at positive angles and thus the ACS effectiveness is not affected. The current control logic for the Attitude Control System during aerobraking commands the thrusters to fire if the attitude is beyond 15° from the freestream direction. Extrapolating the results (using slope

of a curve fit through data points) to beyond 15° is difficult because the reduction of projected area starts to play a role and soon dominates. Interaction effects are not necessarily linear with angle outside of this range. However, an assumption of linearity would reveal that plume-freestream interaction will enhance the restoring moment.

The third situation is the damping of angular rates, such as angular velocity or acceleration. In this case, the thruster would be fired for negative angles of incidence. Negative angles would create a positive restoring aerodynamic moment; the thruster would pulse to create a negative yaw moment to damp the rate of positive angular motion. The net aerodynamic effect, as seen in the figure, is a significantly larger restoring moment. This increase in yaw moment would most likely induce angular motion. This motion would decrease some of the damping gained by firing the thruster. The result is that although the spacecraft remains stable, the effectiveness of the ACS is diminished, possibly increasing the amount of propellant used.

The plume simulation assumes a steady-state condition and does not exactly reproduce flight conditions such as the number of thrusters that are fired and specific impulse, which is a function of propellant tank pressure. However, the simulation does provide strong evidence, along with Magellan mission results, that the situation can occur and should be seriously considered by mission operations.

7.2 Safing Configuration

A DSMC simulation was done to examine the interaction between two thruster plumes and the freestream for the original safing configuration at a freestream density of 120 kg/km^3 . Referring to Figure 7.6, the positions of the two thrusters are on the side opposite the high gain antenna.

Since the only significant interaction between the plumes and freestream occurs for flow at positive incidence, a case was run for flow at an $\alpha = 60^\circ$. This angle was chosen

to compare to the no-jet case previously investigated, and also since transitional effects appear to be greatest near this angle.

The effect of the plume can be seen in Figures 7.7 and 7.8, which display contours of C_p and C_H over the spacecraft in comparison to the no-jet case. The plume creates a shadow over the yoke and half the inboard panel, creating regions of lower pressure and heat transfer coefficients.

Pitching moment coefficient, or moment about Y axis, is plotted against incidence angle in Figure 7.9; the jet and no-jet cases are denoted at 60° . It can be seen that the moment is increased by about 15% with the thrusters fired; that is, the magnitude is decreased, making it less negative.

An angular rate damping analysis demonstrates that the plume will help the effectiveness of the ACS. For an angle of 60° , the natural restoring moment is negative, as seen in the figure. The thrusters in question will fire to create a positive torque about Y in order to damp out the negative rate of angular motion. With thrusters, the resulting aerodynamic moment is lower in magnitude than the original moment. Therefore, the trend is in the direction of reducing the angular rate.

It should be noted that the center of mass location for the analysis of this configuration was not altered from the aerobraking configuration and remained along the Z axis. A realistic center of mass would follow the panels and lie off the Z axis in the direction of the +X axis. This movement would affect the magnitudes of the preceding analysis but not the trends.

8. CONCLUSIONS

The aerodynamics and aerodynamic heating of the Mars Global Surveyor spacecraft have been investigated for a wide range of flight conditions. These results, together with those obtained by other researchers near the conclusion of this study, were used to help design the mission and are currently being utilized to assist mission operations.

The Mars Global Surveyor spacecraft was determined to be aerodynamically stable for flight in both aerobraking and safing configurations. A maximum drag coefficient of 2.13 was calculated for aerobraking at free molecular flow conditions and a value of 1.87 was found for transitional flow at twice the nominal periapsis density. In general, transitional flow effects reduce drag coefficient by about 11% from its free molecular value. In addition, drag coefficient was found to be highly dependent on accommodation coefficient.

The trim angles for both aerobraking and safing configurations are also dependent on the accommodation coefficient. In aerobraking mode, the trim angle will shift almost three degrees for a 20% variation in accommodation coefficient.

Heat transfer is strongly dependent on atmospheric density. Transitional flow effects produce high gradients near the panel edges, creating edges and corners that receive greater heating than the inner regions. These gradients decrease with freestream density. Transitional flow effects are stronger at the outboard panels due to the angular sweep of the panel assembly.

Thruster plume - freestream interaction in the aerobraking configuration reduces drag by 15% and creates thrust reversal. The firing of one thruster may create a net moment opposite in direction to the one intended. Such a reversal is found to be highly dependent on freestream density and begins to occur at about 28 kg/km^3 . Interaction effects will not significantly impact changes in attitude to restore equilibrium, but they will reduce the effectiveness of the Attitude Control System when damping of angular rates is

desired. Plume-freestream interaction effects in the safing configuration will increase the effectiveness of the ACS.

REFERENCES

1. Dallas, S.S., "Mars Global Surveyor Mission", Proceedings of 1997 IEEE Aerospace Conference, Vol.4, Feb. 1-8, 1997, pp.173-189.
2. Cestero, F.J., "An Exploratory Analysis of the Magellan Aerodynamic Characteristics during the Termination Experiment," M.S. Thesis, George Washington University, August 1997.
3. Tolson, R.H., Patterson, M.T., and Lyons, D.T., "Magellan Windmill and Termination Experiments," International Symposium Space Flight Dynamics, CNES, Toulouse, France, June 1995.
4. Espiritu, R.C., and Tolson, R.H., "Determining Venusian Upper Atmosphere Characteristics Using Magellan Attitude Control Data," AAS Paper 95-152, February 1995.
5. Rault, D.F., "Aerodynamic Characteristics of the Magellan Spacecraft in the Venus Upper Atmosphere," Journal of Spacecraft and Rockets, Vol. 31, No. 4, July 1994, pp. 537-542.
6. Lyons, D.T., "Aerobraking Magellan: Plan versus Reality," Advances in the Astronautic Sciences, 87, part II, 1994, pp. 663-680.
7. Bird, G.A., *Molecular Gas Dynamics*, Clarendon Press, Oxford, 1976.
8. Bird, G.A., *Molecular Gas Dynamics and the Direct Simulation of Gas Flows*, Clarendon Press, Oxford, 1994.
9. Haas, B., "Flow Resolution and Domain Influence in Rarefied Hypersonic Blunt-Body flows," AIAA Paper 93-2806, July 1993.
10. Rault, D.F., "Aerodynamic Characteristics of the Shuttle Orbiter at High Altitudes," *Journal of Spacecraft and Rockets*, Vol. 31, No. 6, Nov. 1994, pp. 944 - 952.
11. Rault, D.F., Cestero, F.J., and Shane, R.W., "Spacecraft Aerodynamics During Aerobraking Maneuver in Planetary Atmospheres," AIAA Paper 96-1890, June 1996.
12. Rault, D.F., "RCS Plume Effect on Spacecraft Aerodynamics During Aerobraking Maneuver," 20th International Symposium on Rarefied Gas Dynamics, Institute of Mechanics, CAS, Beijing, China, August 1996.
13. Woronowicz, M.S. and Rault, D.F., "Direct Simulation Monte Carlo Prediction of On-Orbit Contaminant Deposit Levels for HALOE," NASA TM 109069, August 1994.
14. Beguelin, A., Dongarra, J., Geist, A., Manchek, R., and Sunderam, V., "A User's Guide to PVM Parallel Virtual Machine," Oak Ridge National Lab., ORNL/TM-11826, July 1991.

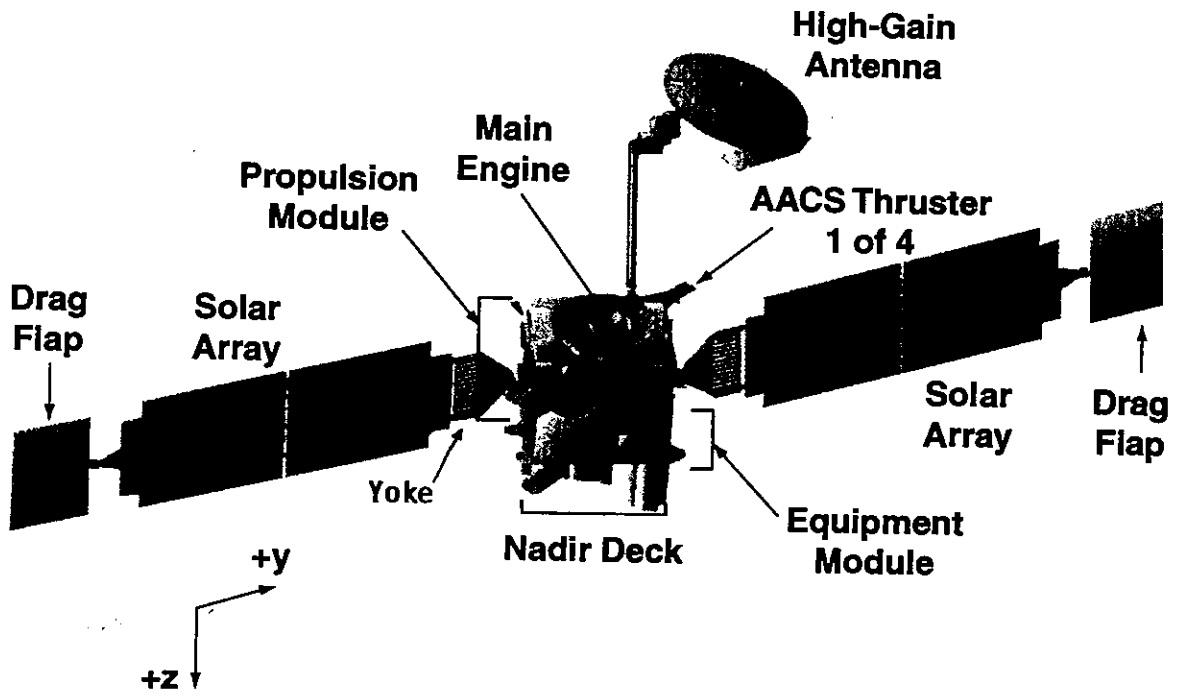


Figure 2.1. Mars Global Surveyor spacecraft.

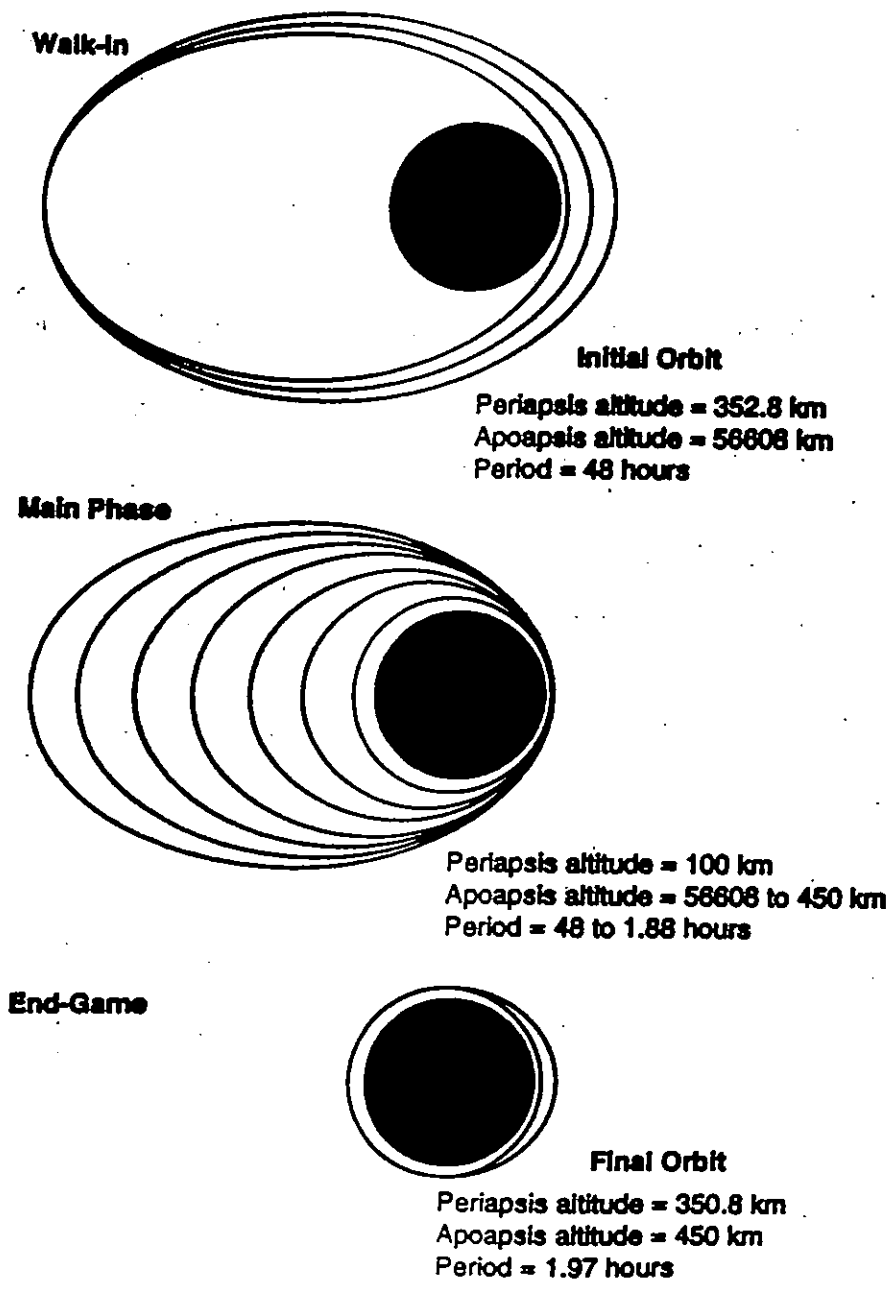


Figure 3.1. Original aerobraking scenario.

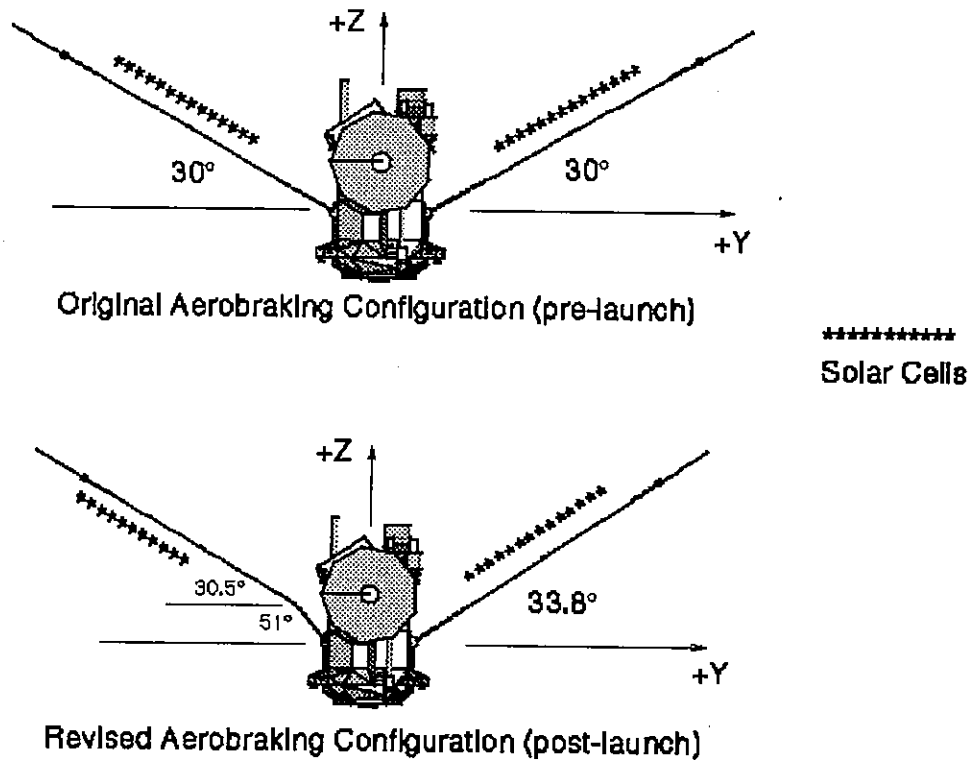


Figure 3.2. MGS aerobraking configurations, original and revised.

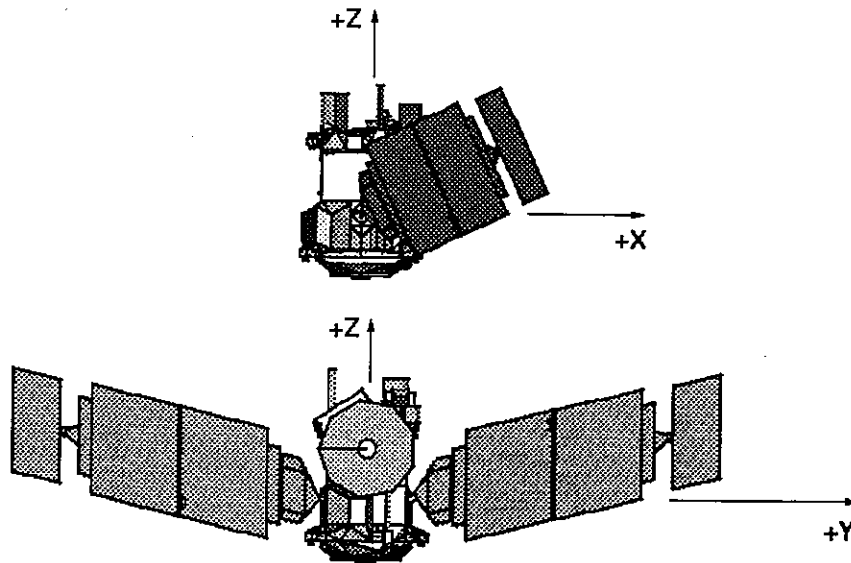


Figure 3.3 MGS safing configuration.

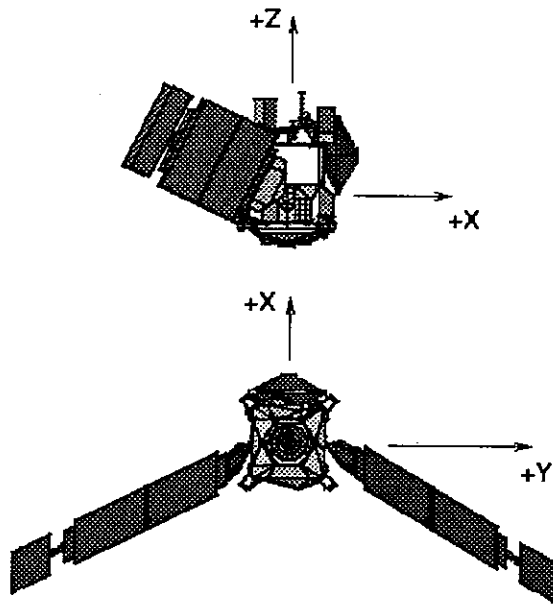


Figure 3.4. MGS revised safing configuration.

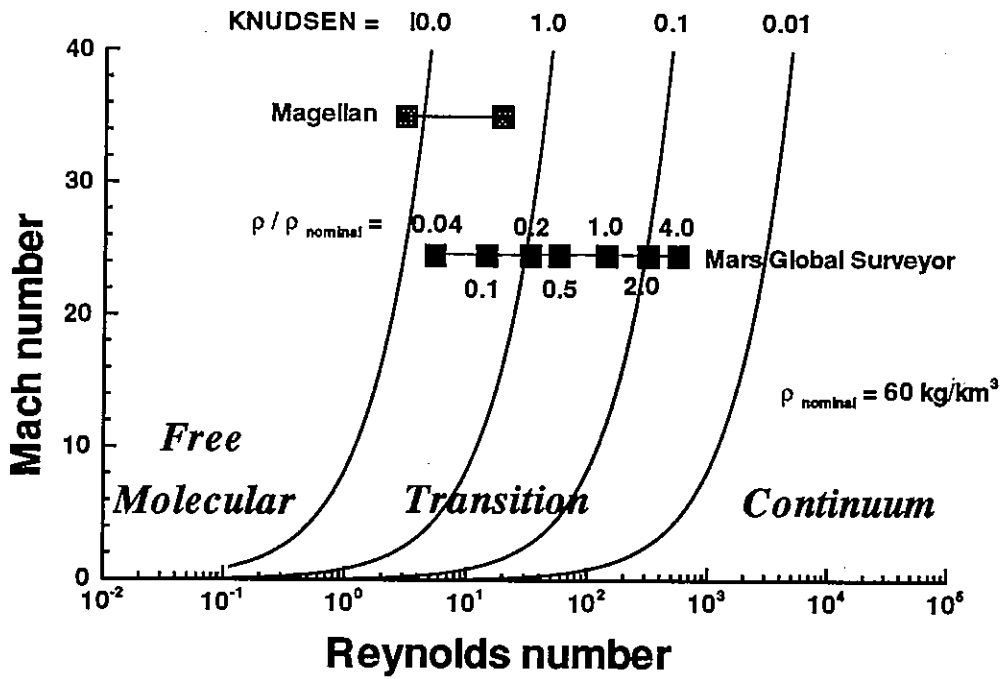


Figure 4.1. Flow regimes for aerobraking maneuvers.

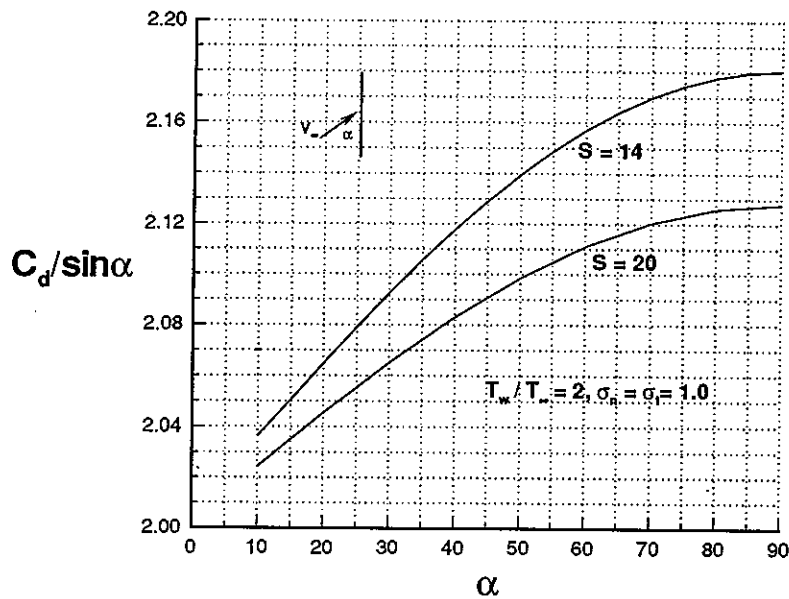


Figure 4.2. Flat plate drag coefficient for various speed ratios.

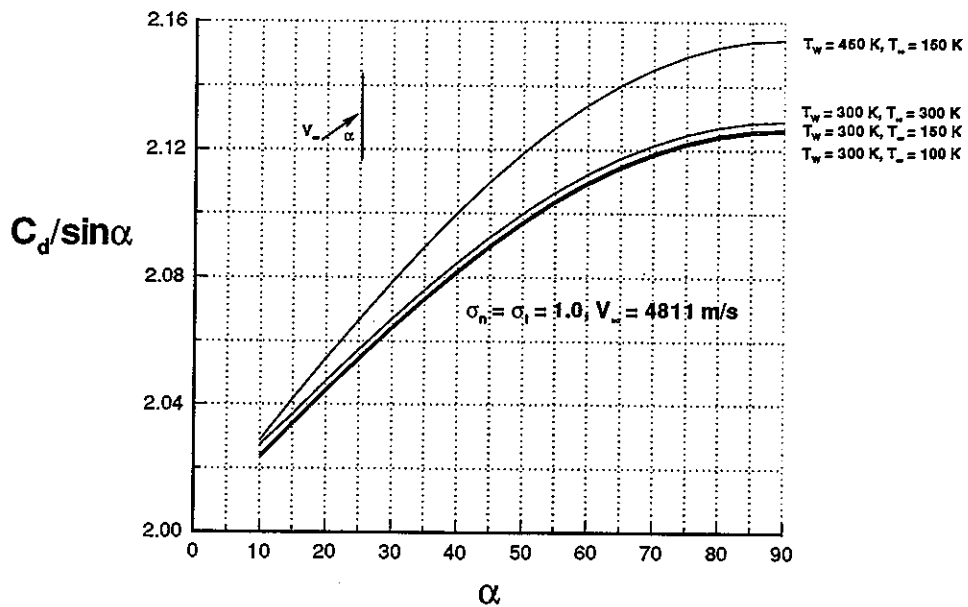


Figure 4.3. Flat plate drag coefficient for various temperatures.

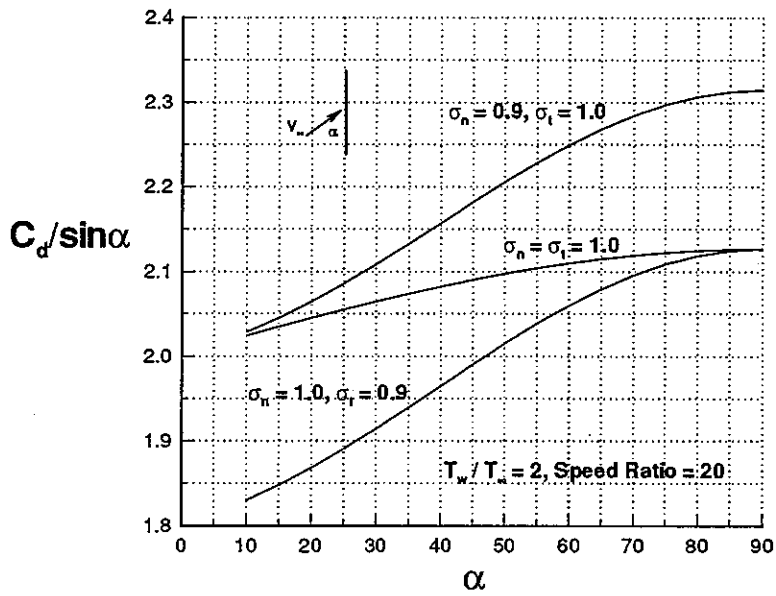


Figure 4.4. Flat plate drag coefficient for various accommodation coefficients.

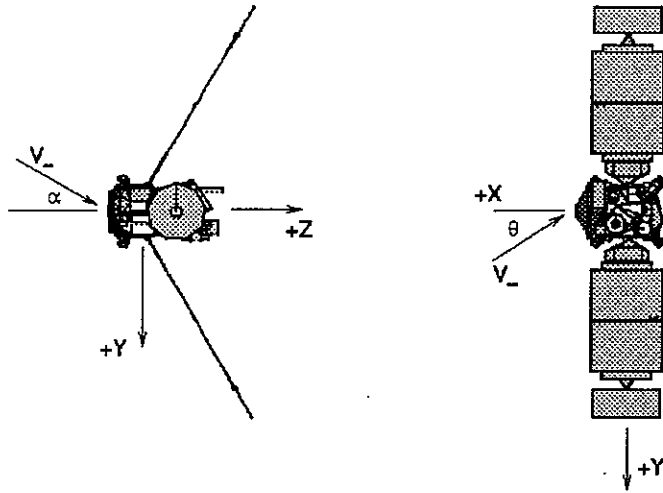


Figure 5.1. Freestream angle of incidence reference system, aerobraking configuration.

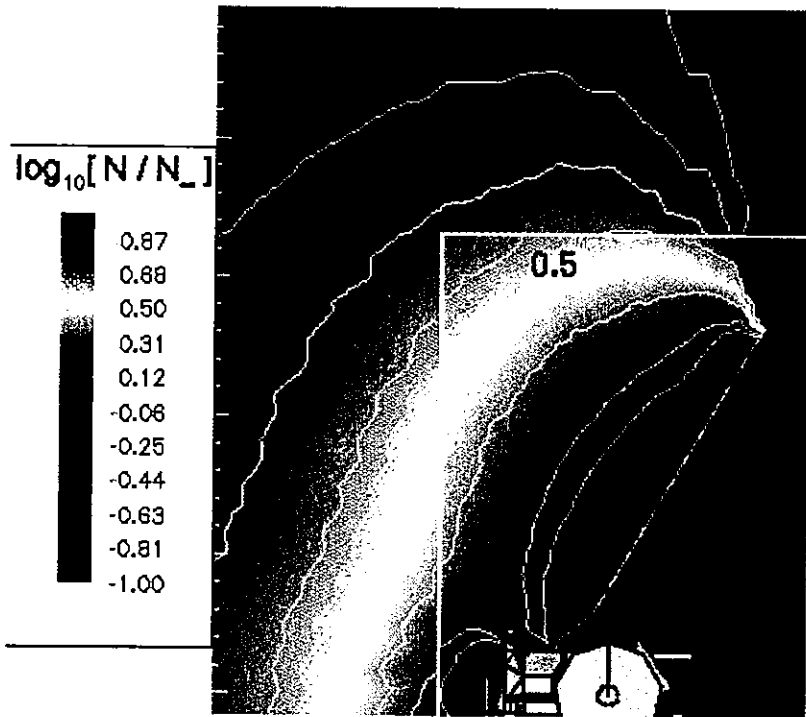


Figure 5.2. Density contours for free molecular flow field.

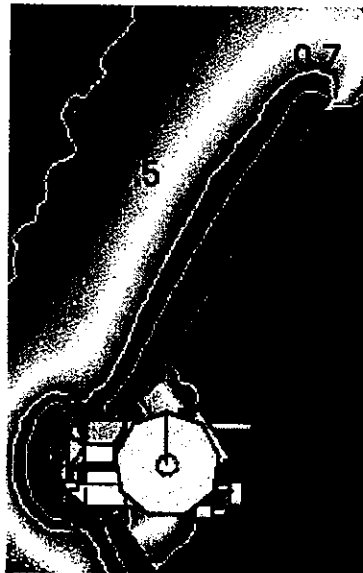
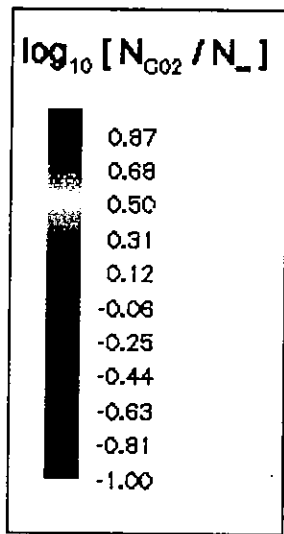


Figure 5.3. Density contours for transitional flow field.

Angle	Angle	CFX	CFX	CFY	CFY	CFZ	CFZ
α	θ	DSMC	Free Mol	DSMC	Free Mol	DSMC	Free Mol
0	0	-0.007	-0.006	-0.003	0.000	1.98	2.15
-10	0	-0.008	-0.001	-0.30	-0.36	1.90	2.12
-15	15	0.065	0.13	-0.43	-0.51	1.82	2.06
15	15	0.066	0.13	0.42	0.51	1.82	2.06
-30	0	-0.009	-0.001	-0.78	-0.95	1.50	1.66
30	0	-0.008	-0.001	0.78	0.95	1.50	1.66
-15	90	0.285	0.514	-0.002	0.000	1.9	1.98
15	90	-0.309	-0.53	-0.004	0.000	1.9	2.06
-30	90	0.586	0.950	-0.002	0.000	1.66	1.66

Reference Area = 17.5 m²
 $\rho = 120 \text{ kg/km}^3$

Table 1. Force coefficients for aerobraking configuration.

Angle	Angle	CMX	CMX	CMY	CMY	CMZ	CMZ
α	θ	DSMC	Free Mol	DSMC	Free Mol	DSMC	Free Mol
0	0	0.003	-0.007	-0.001	-0.001	0.000	0.000
-10	0	0.092	0.092	-0.001	-0.007	-0.001	-0.001
-15	15	0.13	0.13	-0.005	0.006	0.003	-0.007
15	15	-0.12	-0.13	0.005	0.006	0.002	0.007
-30	0	0.246	0.238	-0.001	-0.007	-0.002	-0.004
30	0	-0.238	-0.238	-0.001	-0.006	0.001	0.003
-15	90	0.003	-0.001	0.023	0.044	0.000	0.000
15	90	0.003	-0.001	-0.025	-0.053	0.000	0.000
-30	90	0.003	-0.001	0.046	0.077	-0.001	0.000

Reference Area = 17.5 m²
 Reference Length = 9 m
 $\rho = 120 \text{ kg/km}^3$

Table 2. Moment coefficients for aerobraking configuration.

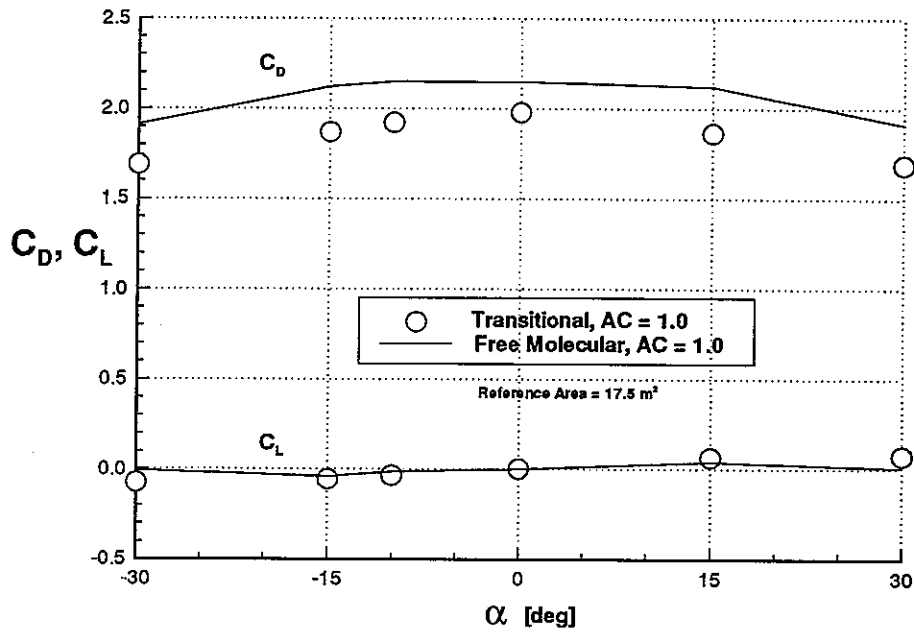


Figure 5.4. Drag and lift coefficients vs. yaw angle, aerobraking configuration.

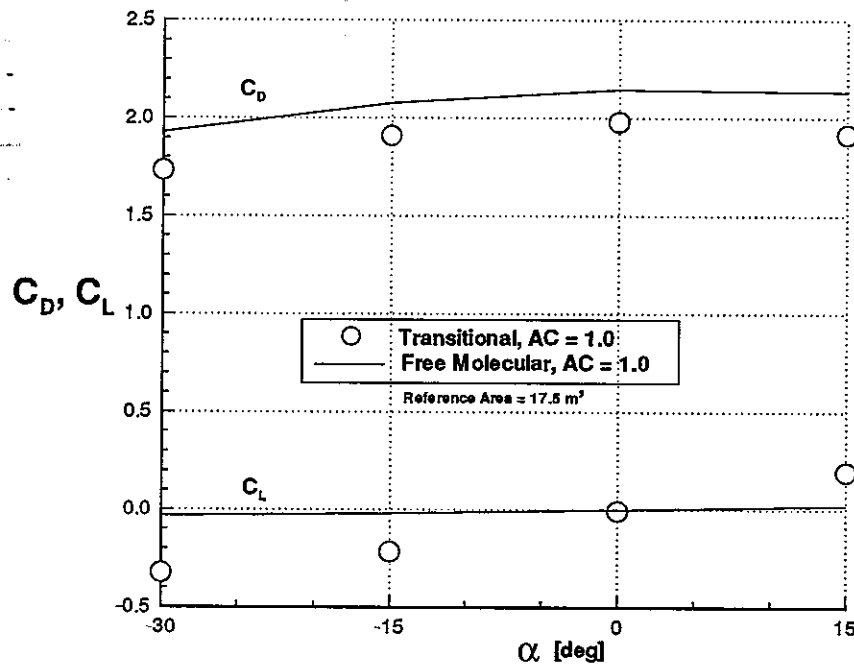


Figure 5.5 Drag and lift coefficients vs. pitch angle, aerobraking configuration.

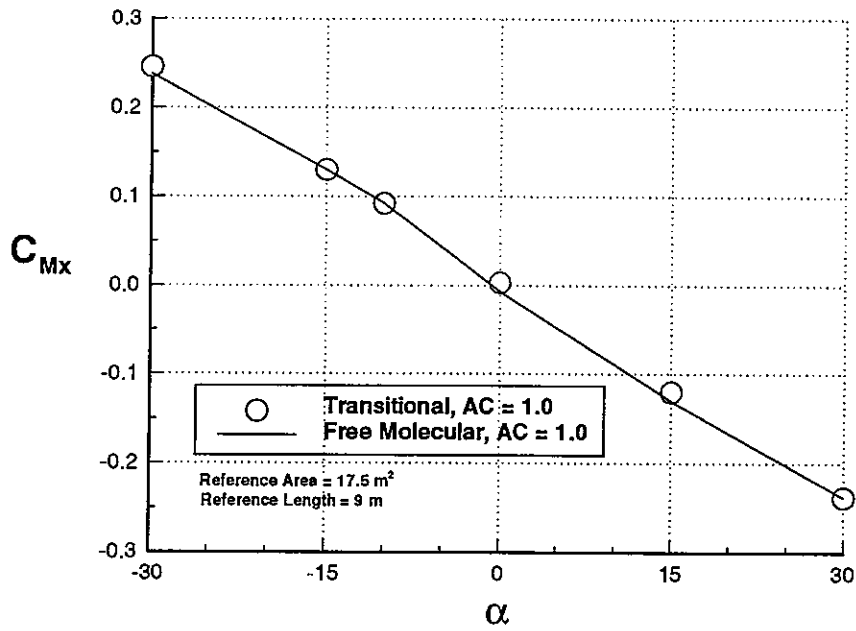


Figure 5.6. Moment coefficients vs. yaw angle, aerobraking configuration.

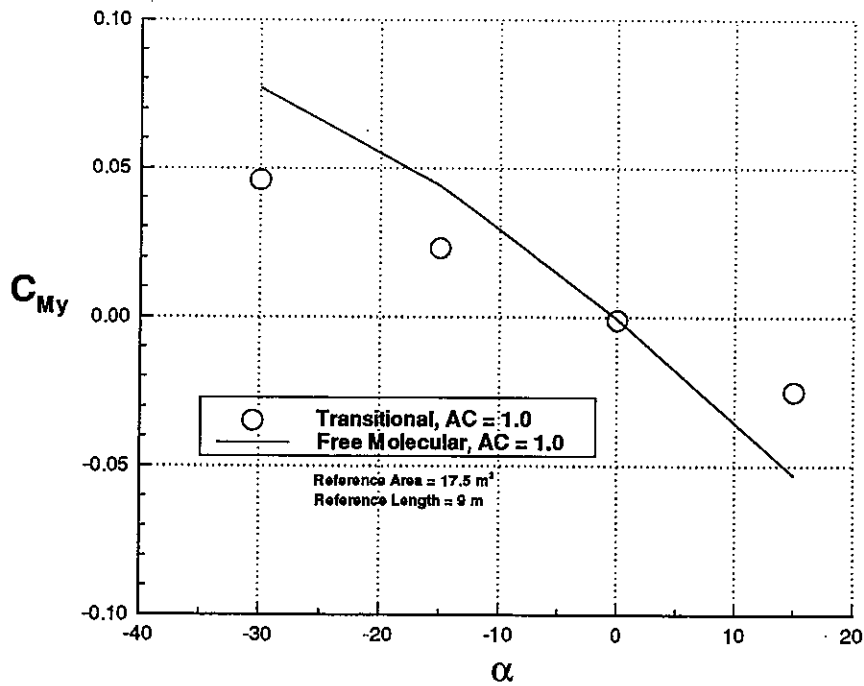


Figure 5.7. Moment coefficients vs. pitch angle, aerobraking configuration.

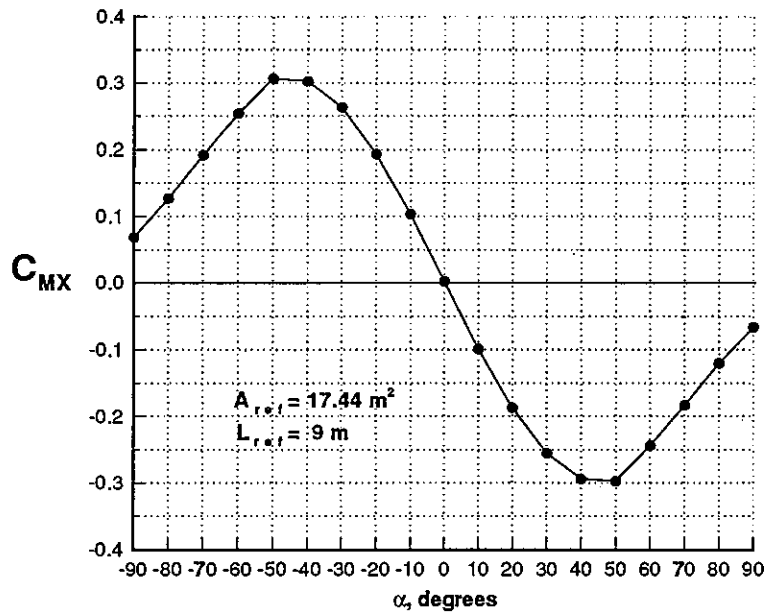


Figure 5.8. Free molecular moment coefficients vs. yaw angle, revised aerobraking.

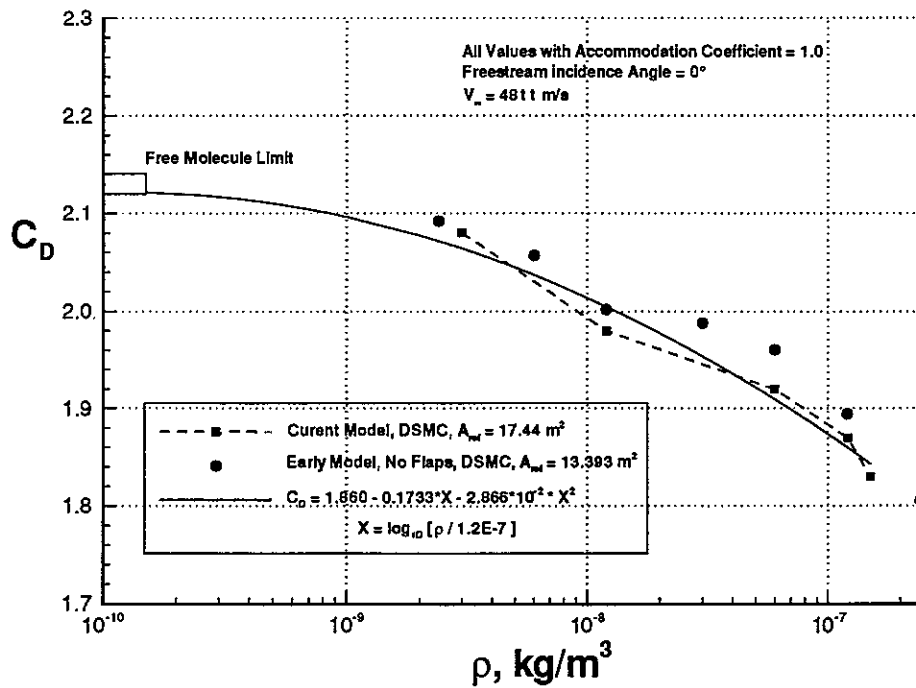


Figure 5.9. Drag coefficient as function of density for various models.

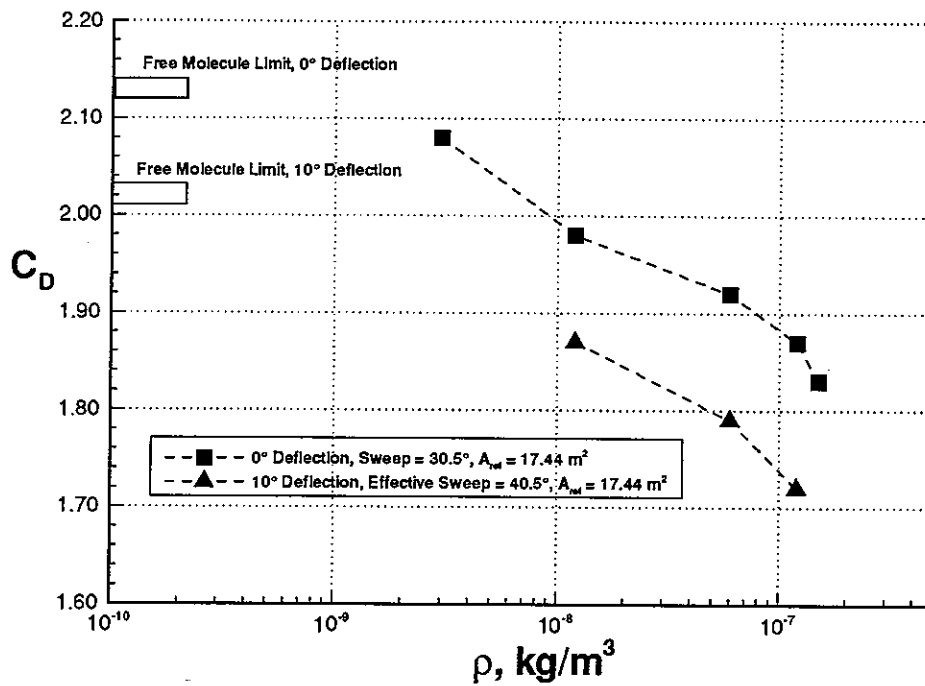


Figure 5.10. Drag coefficient normalized by baseline area for various deflections.

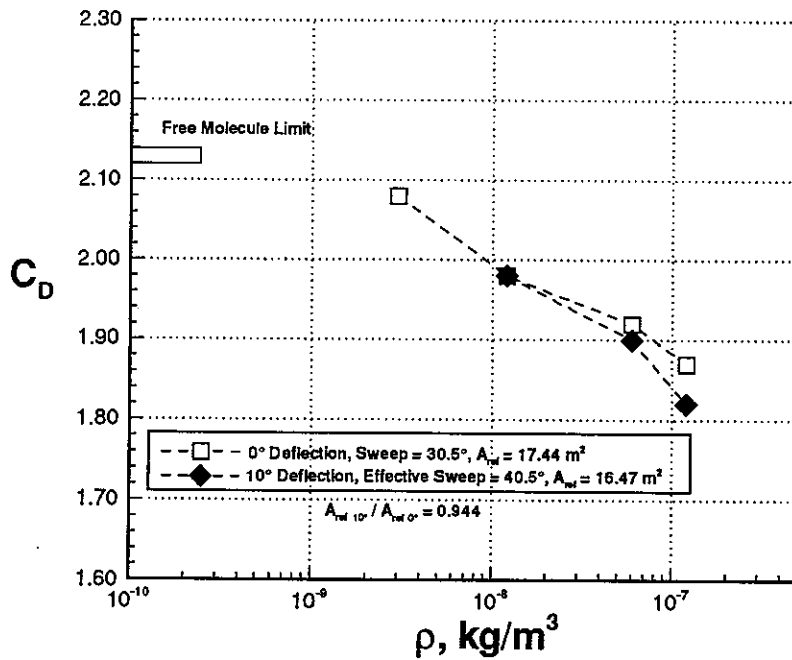


Figure 5.11. Drag coefficient normalized by respective areas for various deflections.

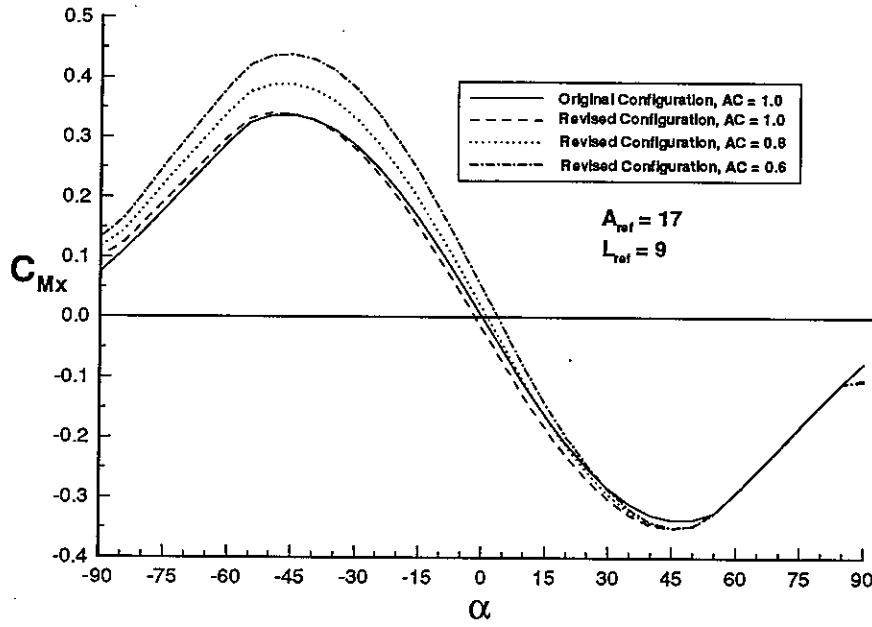


Figure 5.12. Moment coefficients for various panel accommodation coefficients.

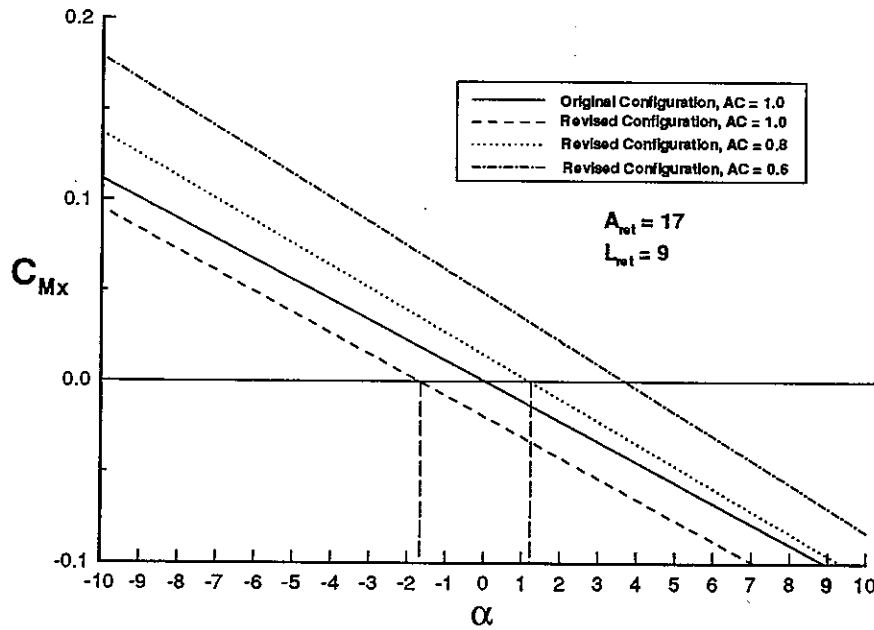


Figure 5.13. Moment coefficients for various panel accommodation coefficients, detail.

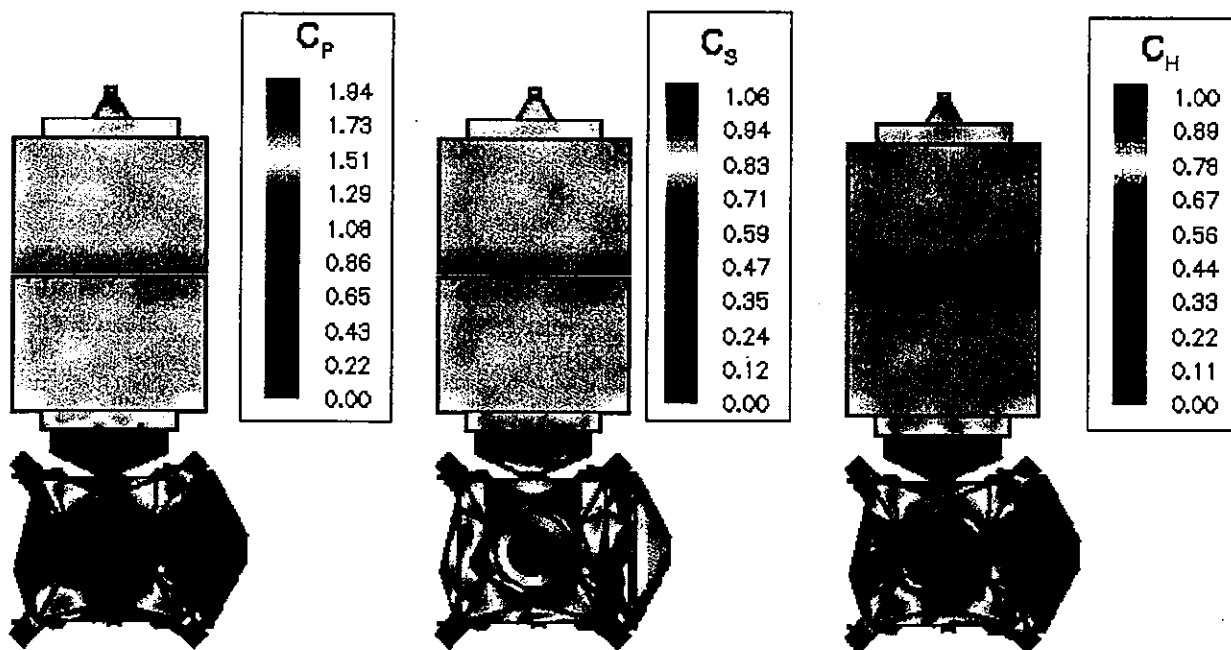


Figure 5.14. Pressure, shear, and heat transfer contours for free molecular flow.

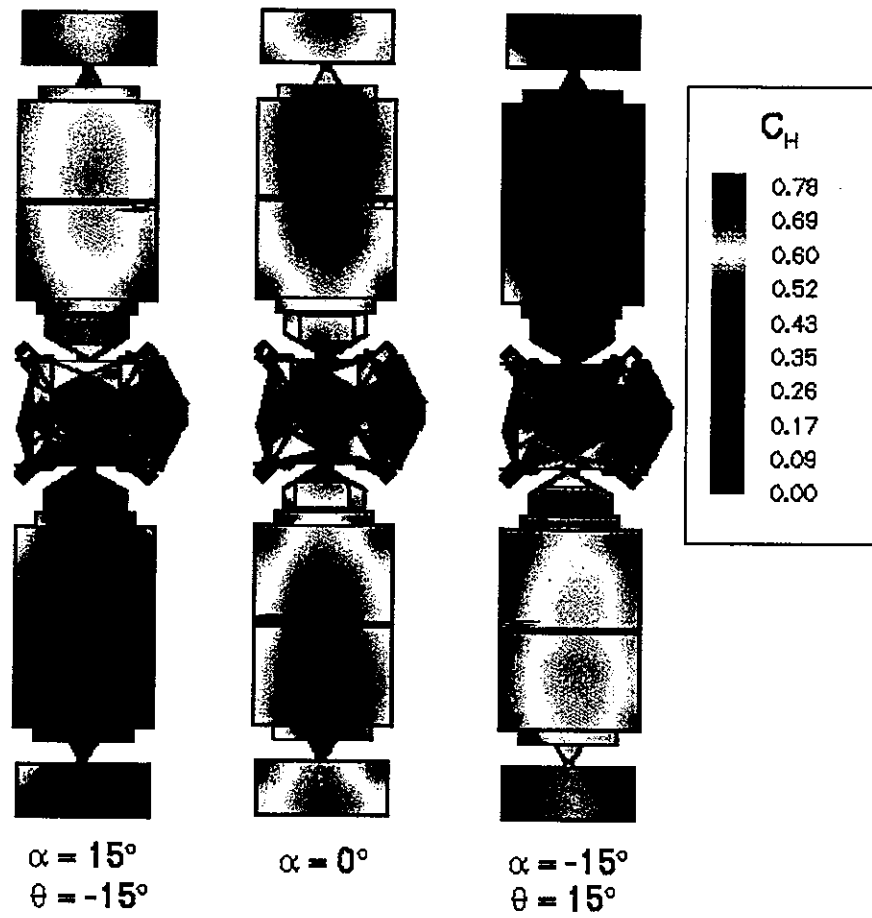


Figure 5.15. Heat transfer coefficient contours for transitional flow.

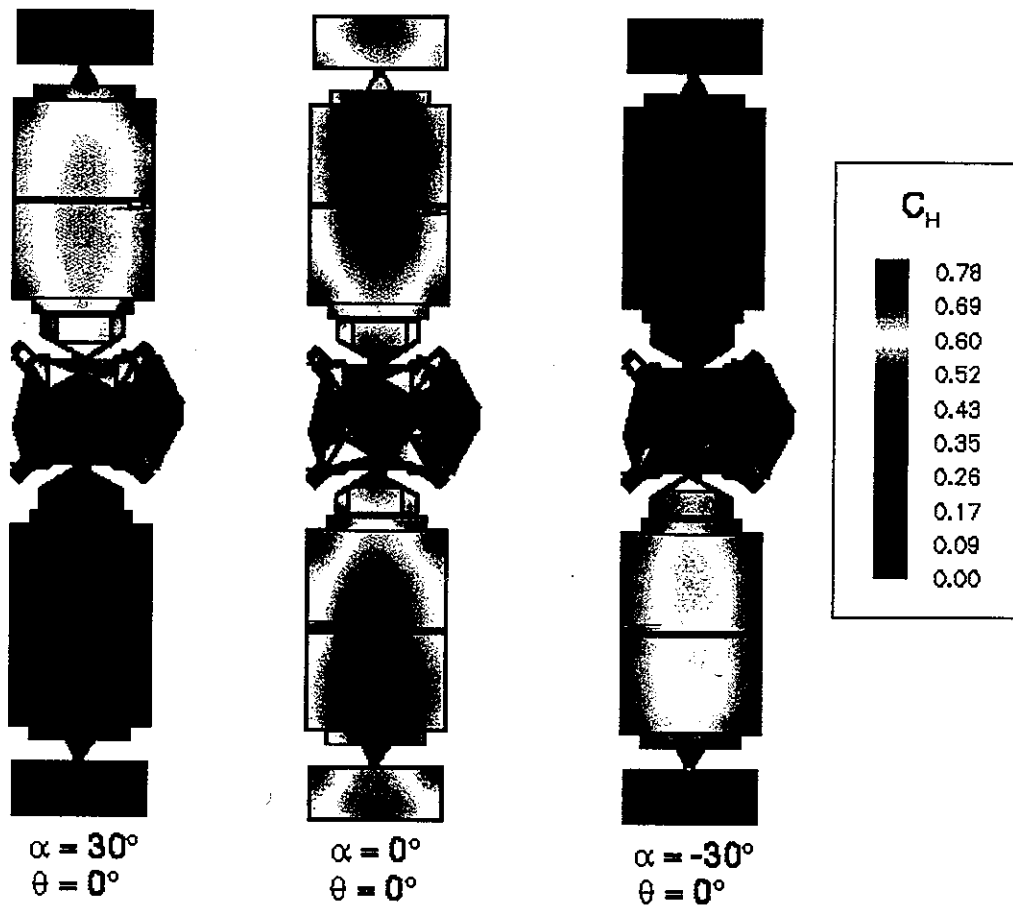


Figure 5.16. Heat transfer coefficient contours.

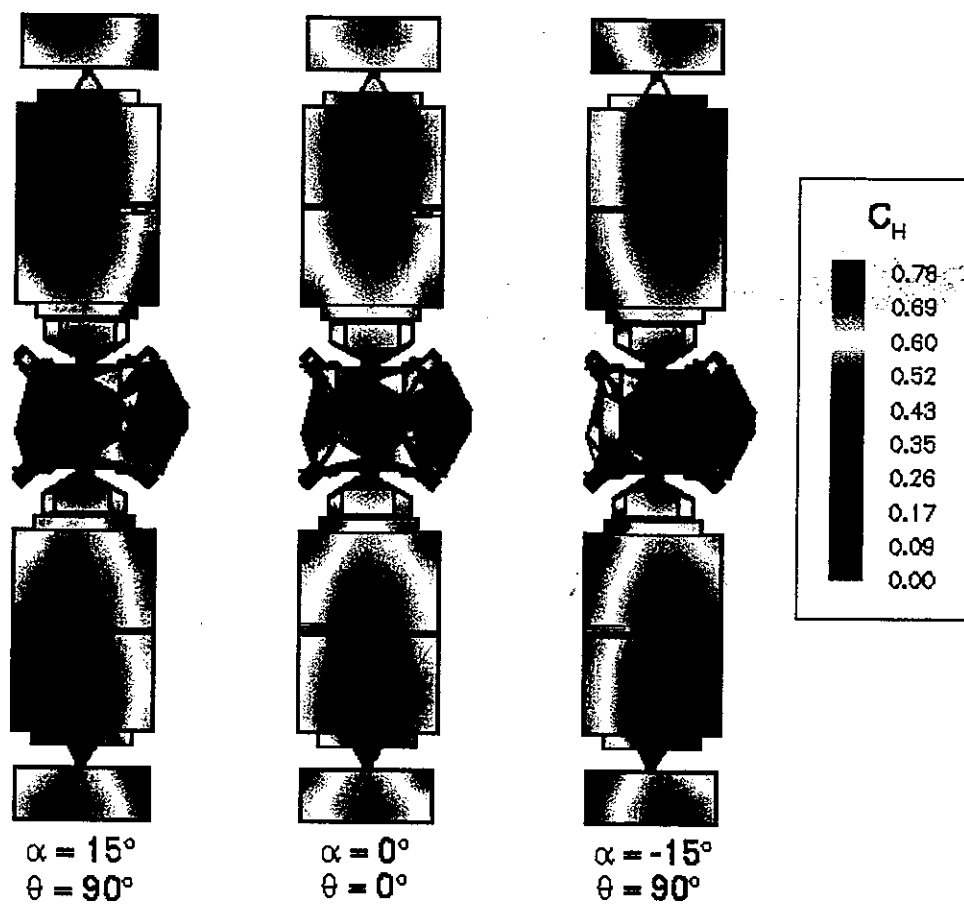


Figure 5.17. Heat transfer coefficient contours.

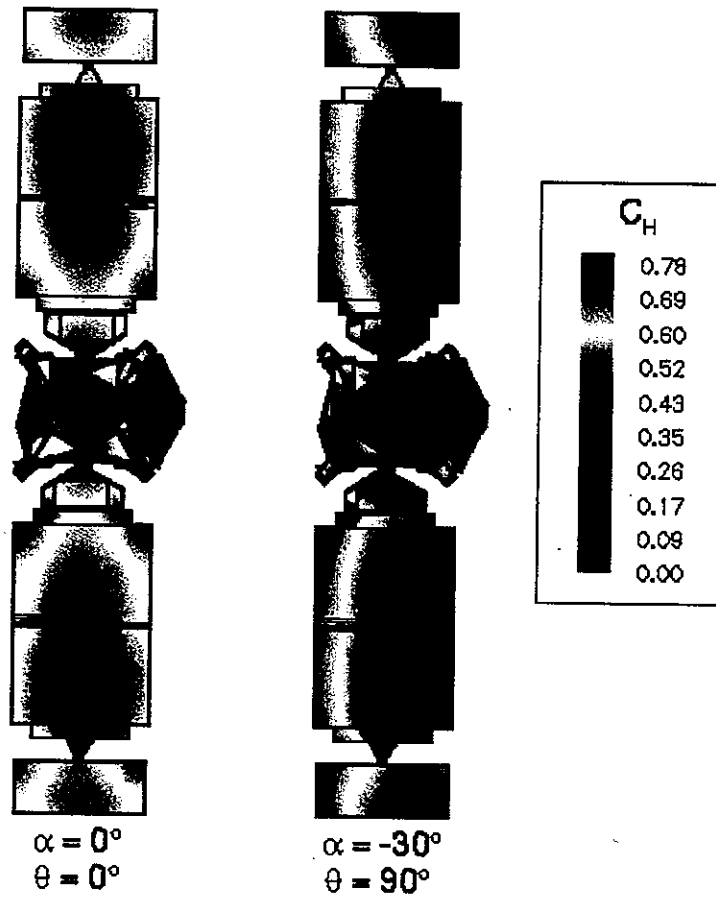


Figure 5.18. Heat transfer coefficient contours.

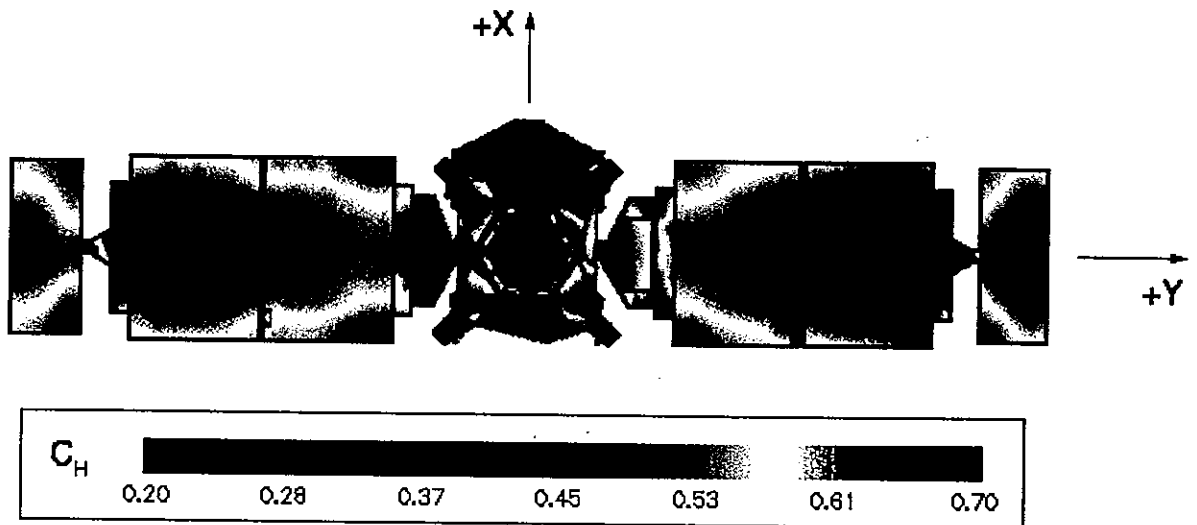


Figure 5.19. Heat transfer coefficient contours for revised aerobraking configuration.

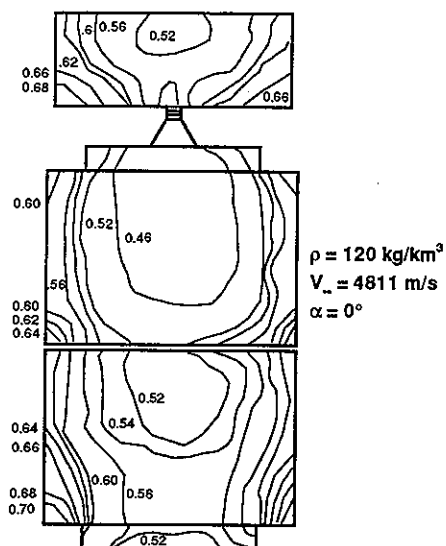


Figure 5.20. Heat transfer coefficient contour lines for revised aerobraking configuration.

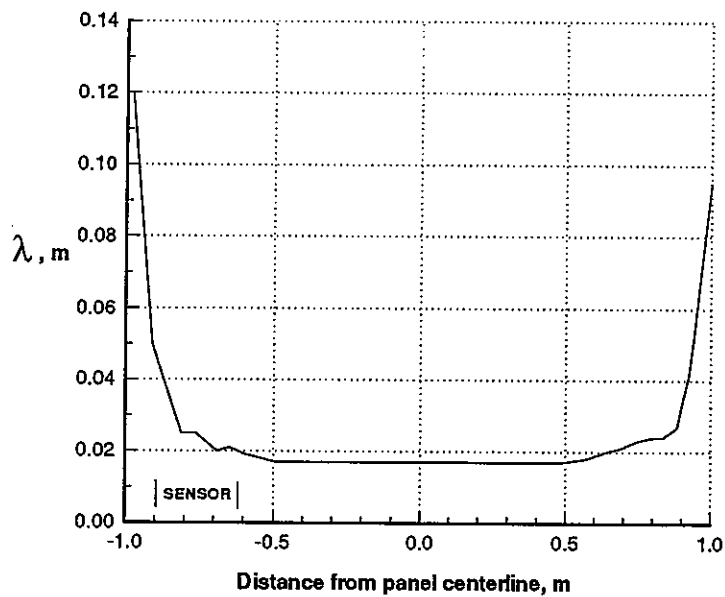


Figure 5.21. Mean free path above sensor.

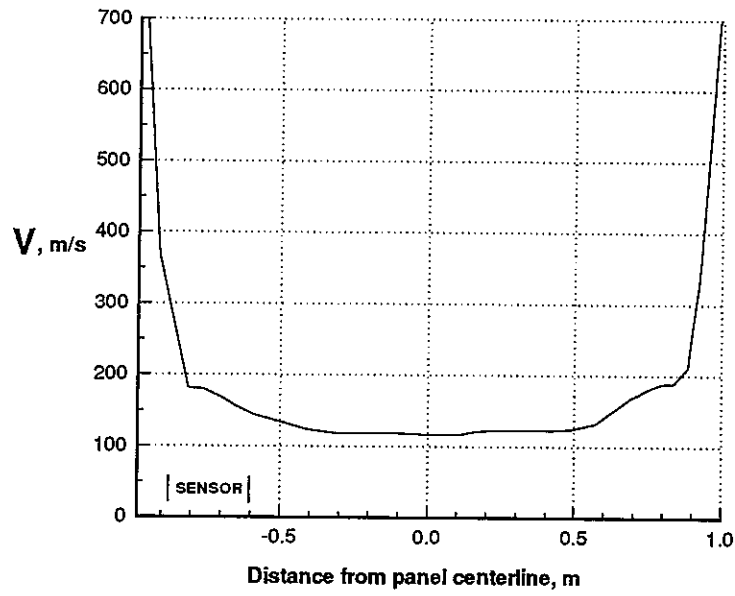


Figure 5.22. Velocity magnitude above sensor.

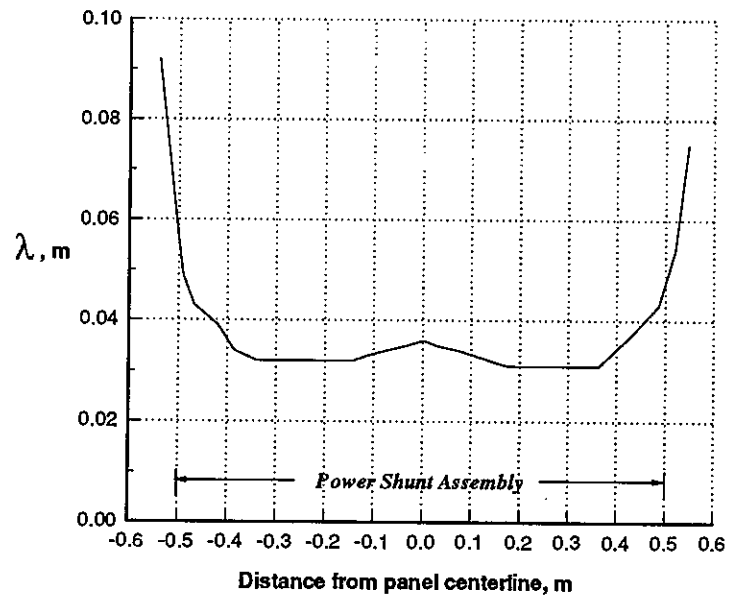


Figure 5.23. Mean free path above power shunt.

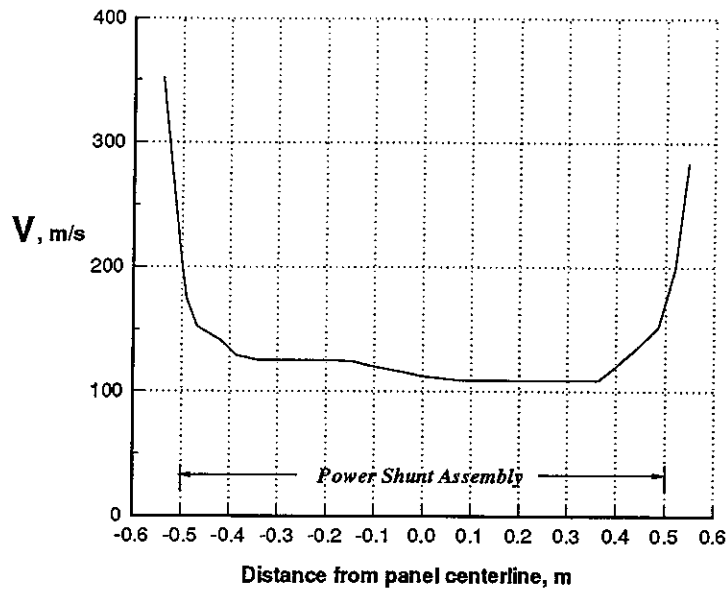


Figure 5.24. Velocity magnitude above power shunt.

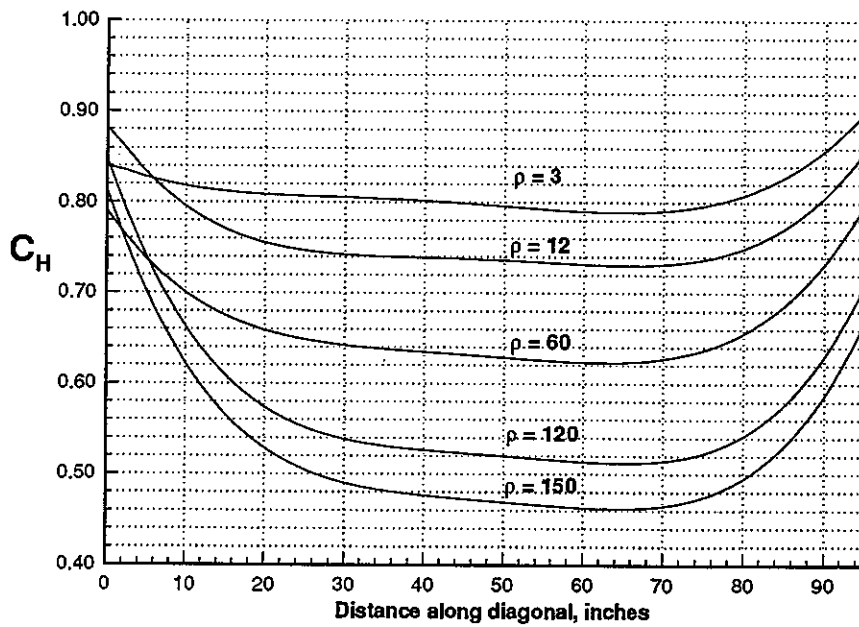


Figure 5.25. Heat transfer coefficient along panel diagonal for various densities.



Figure 5.26. Location of inboard and outboard panel diagonals.

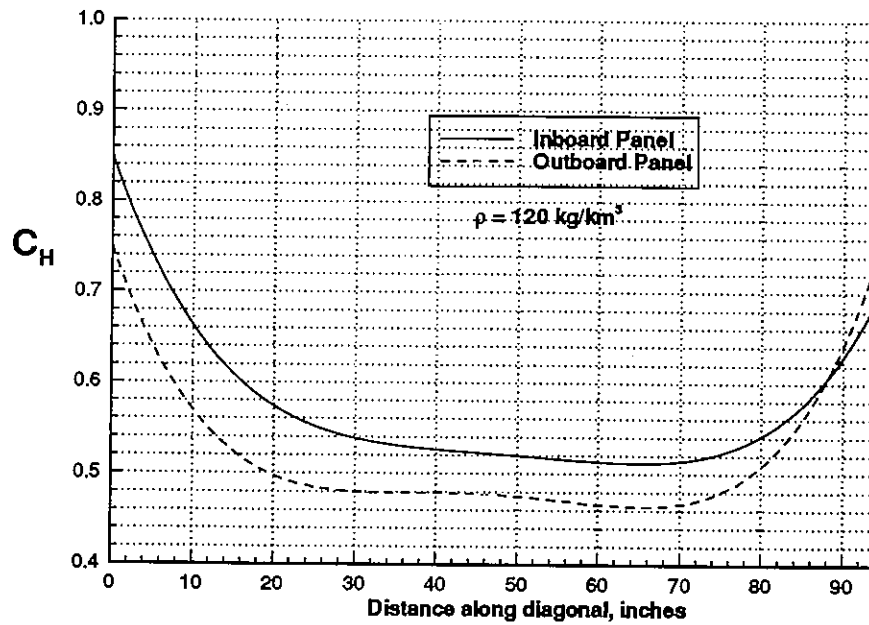


Figure 5.27. Heat transfer coefficient along panel diagonals, $\rho = 120 \text{ kg/km}^3$.

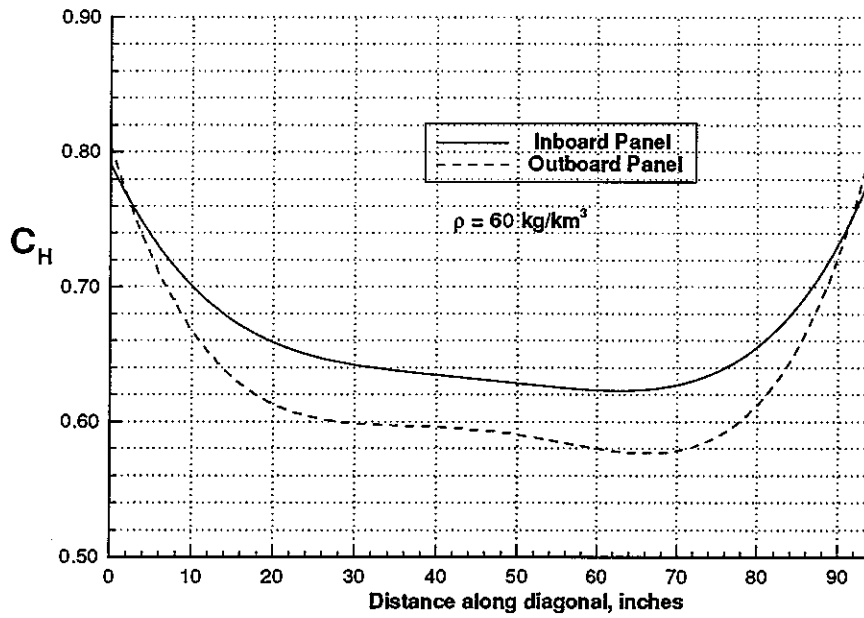


Figure 5.28. Heat transfer coefficient along panel diagonals, $\rho = 60 \text{ kg/km}^3$.

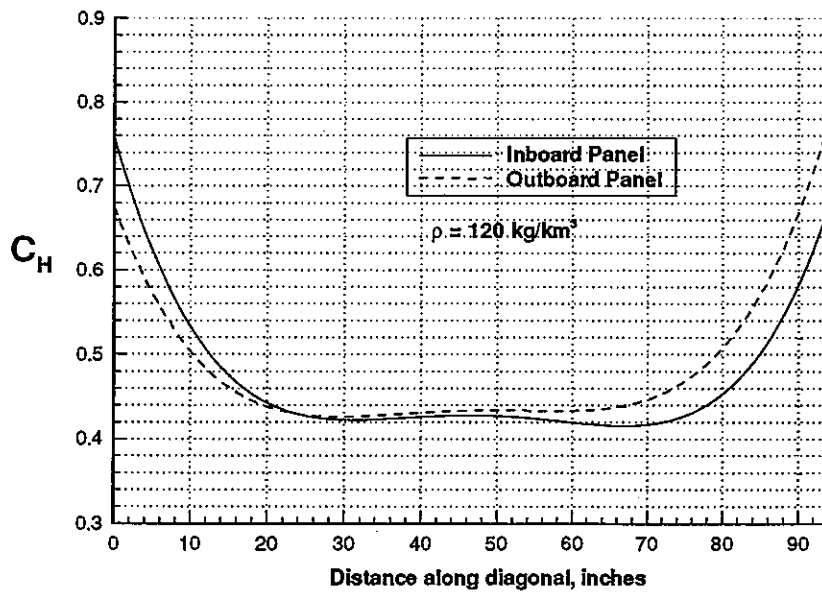


Figure 5.29. Heat transfer coefficient along panel diagonals; -Y panel along -Y axis.

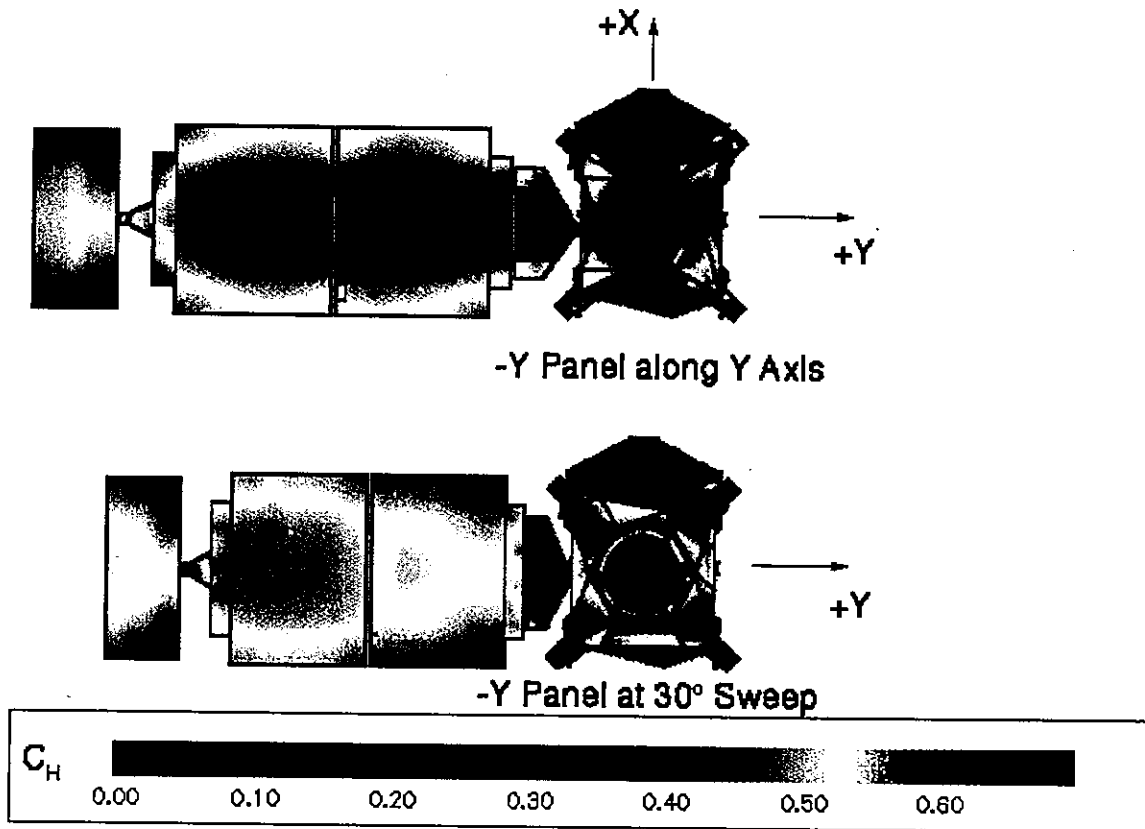


Figure 5.30. Heat transfer coefficient contours, 0° and 30° panel sweeps.

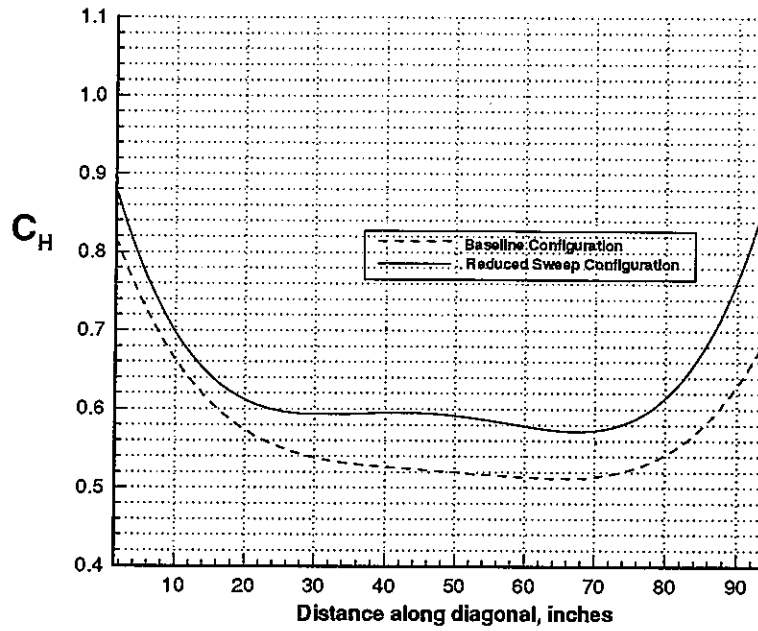


Figure 5.31. Heat transfer coefficient along -Y inboard diagonal.

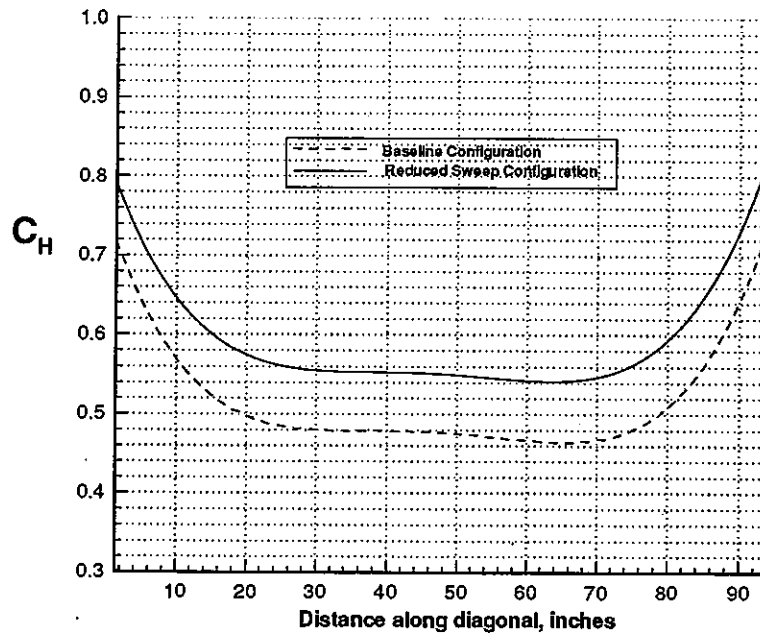


Figure 5.32 Heat transfer coefficient along -Y outboard diagonal.

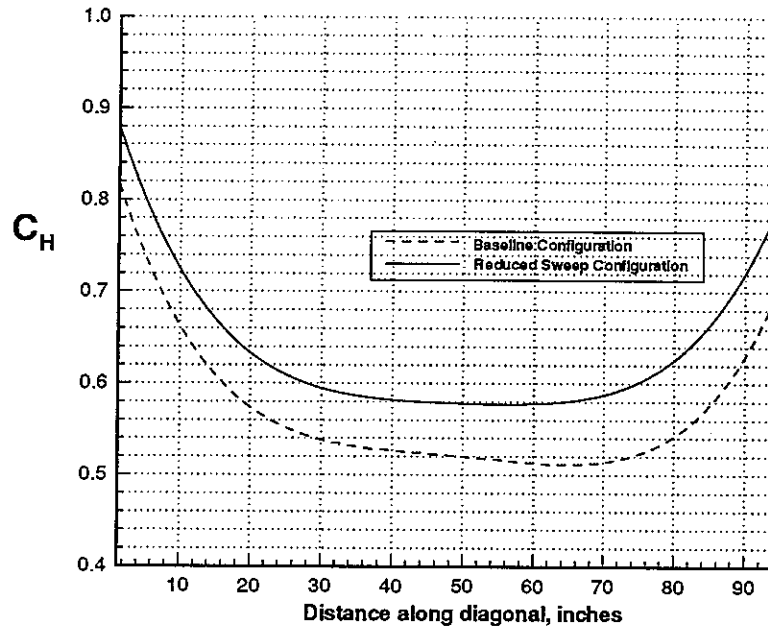


Figure 5.33 Heat transfer coefficient along +Y inboard diagonal.

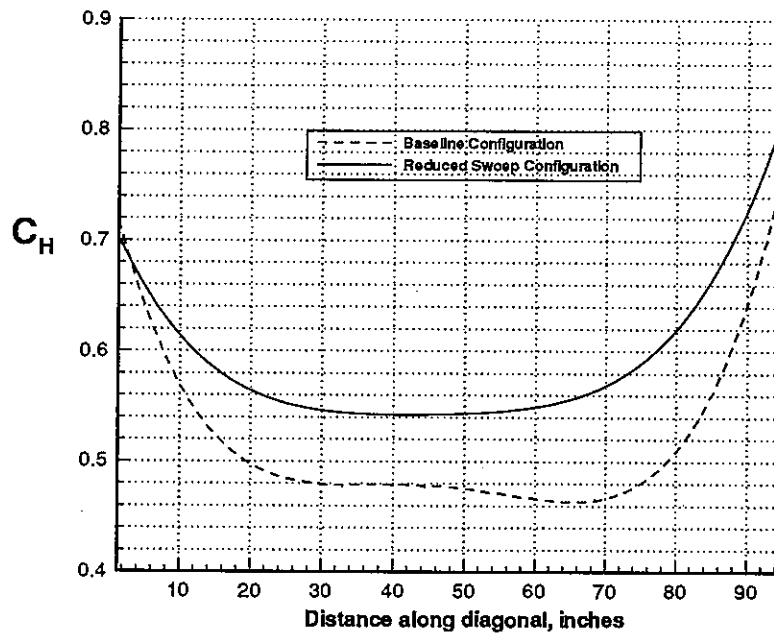


Figure 5.34. Heat transfer coefficient along +Y outboard diagonal.

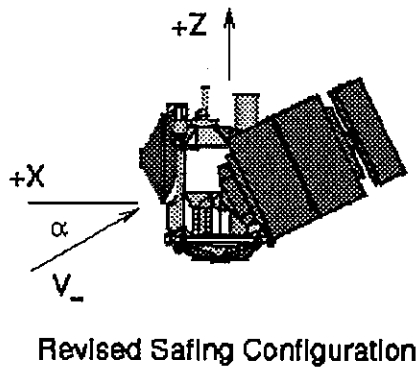
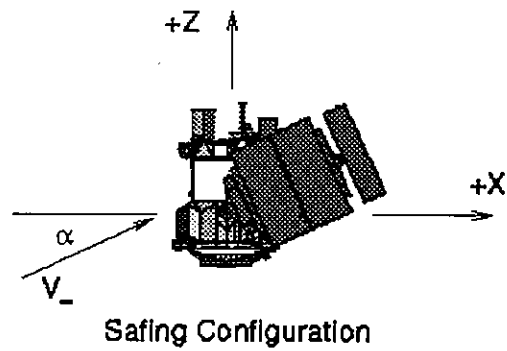


Figure 6.1. Freestream incidence angle reference system for safing configuration.

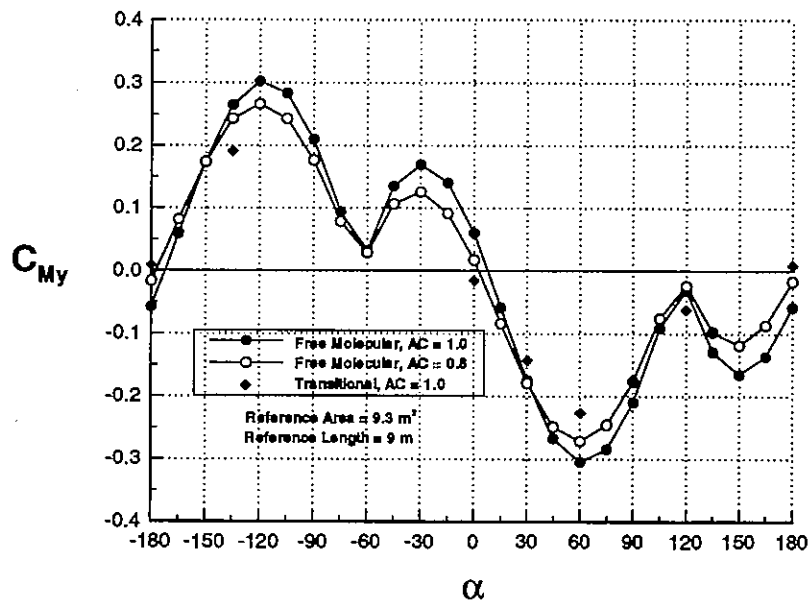


Figure 6.2 Moment coefficients for pitch angle, safing configuration.

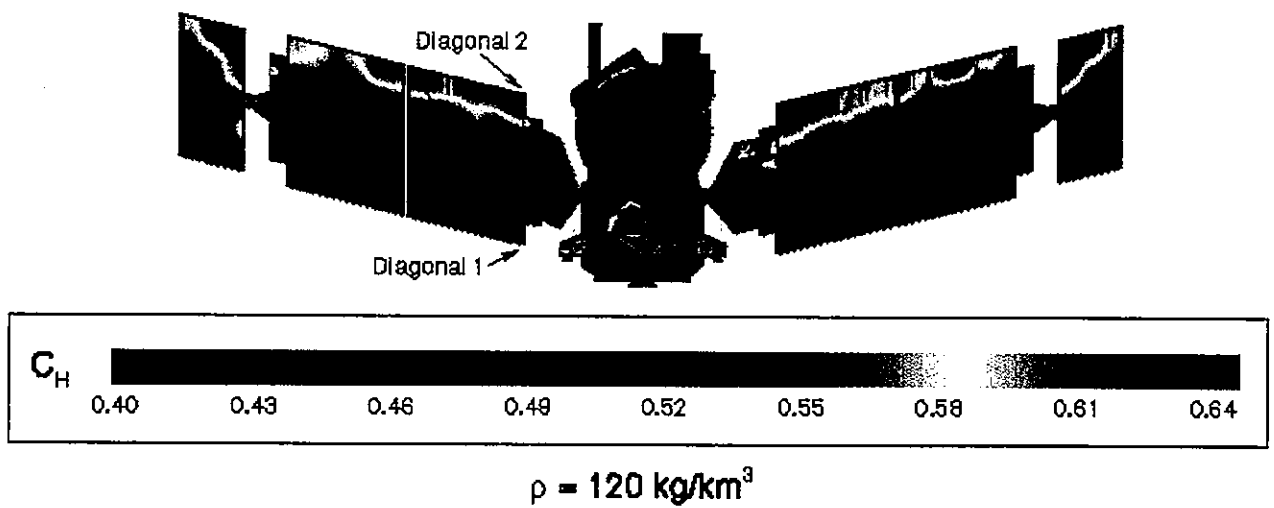


Figure 6.3. Heat transfer coefficient contours, revised safing configuration.

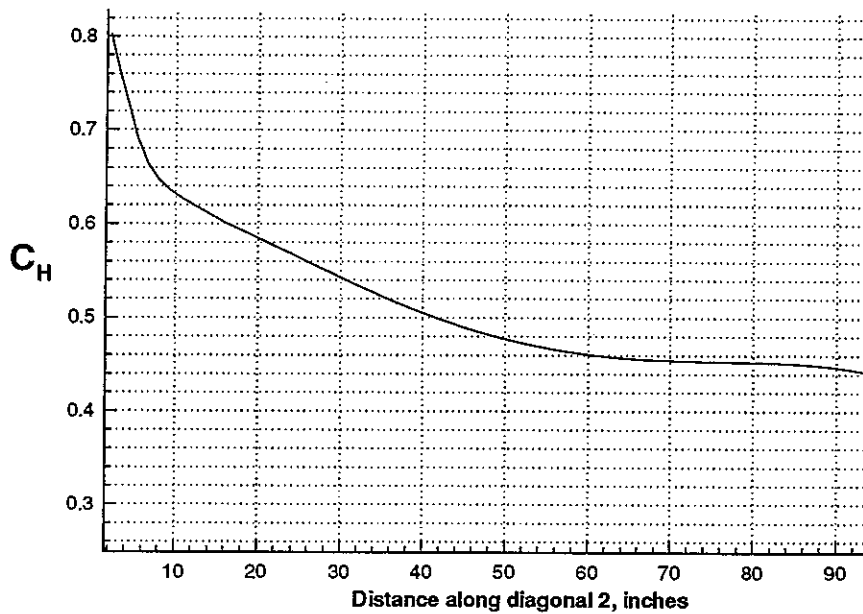


Figure 6.4. Heat transfer coefficient along inner panel diagonal, revised safing configuration.

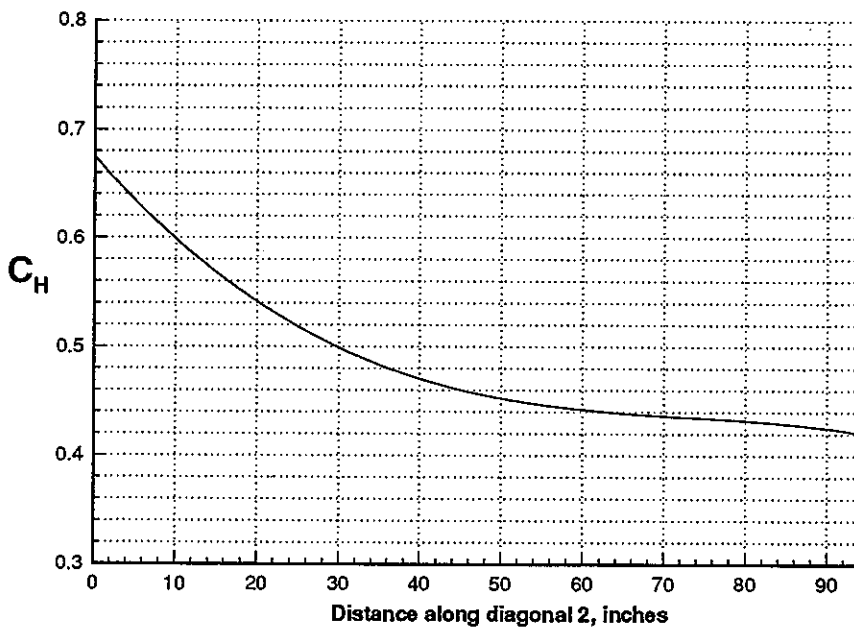


Figure 6.5. Heat transfer coefficient along outer panel diagonal; revised safing configuration.

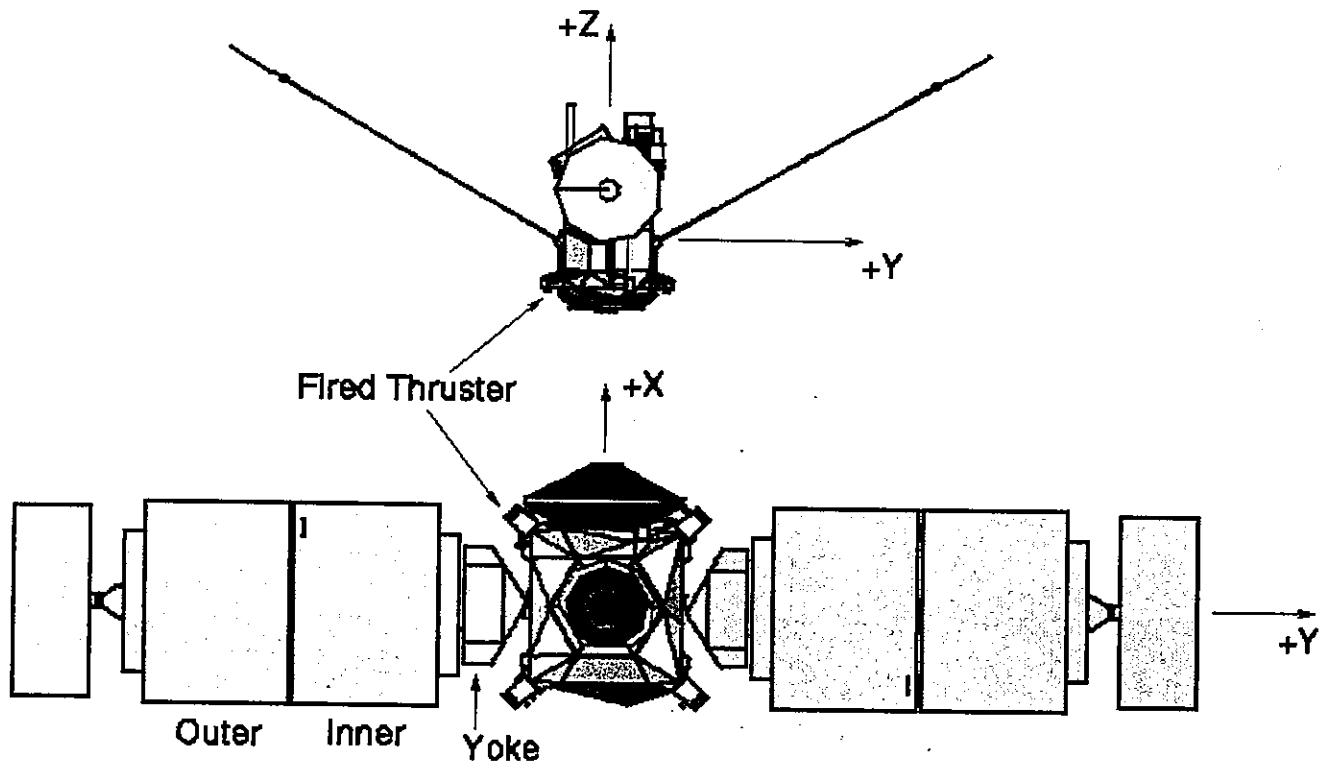


Figure 7.1. Location of simulated thruster plume, aerobraking configuration.

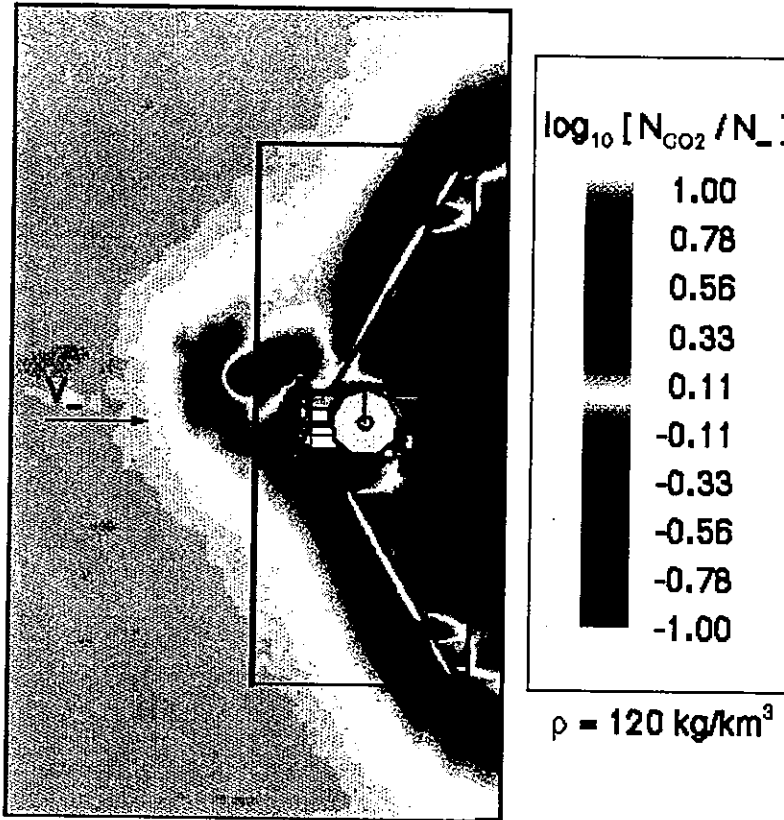
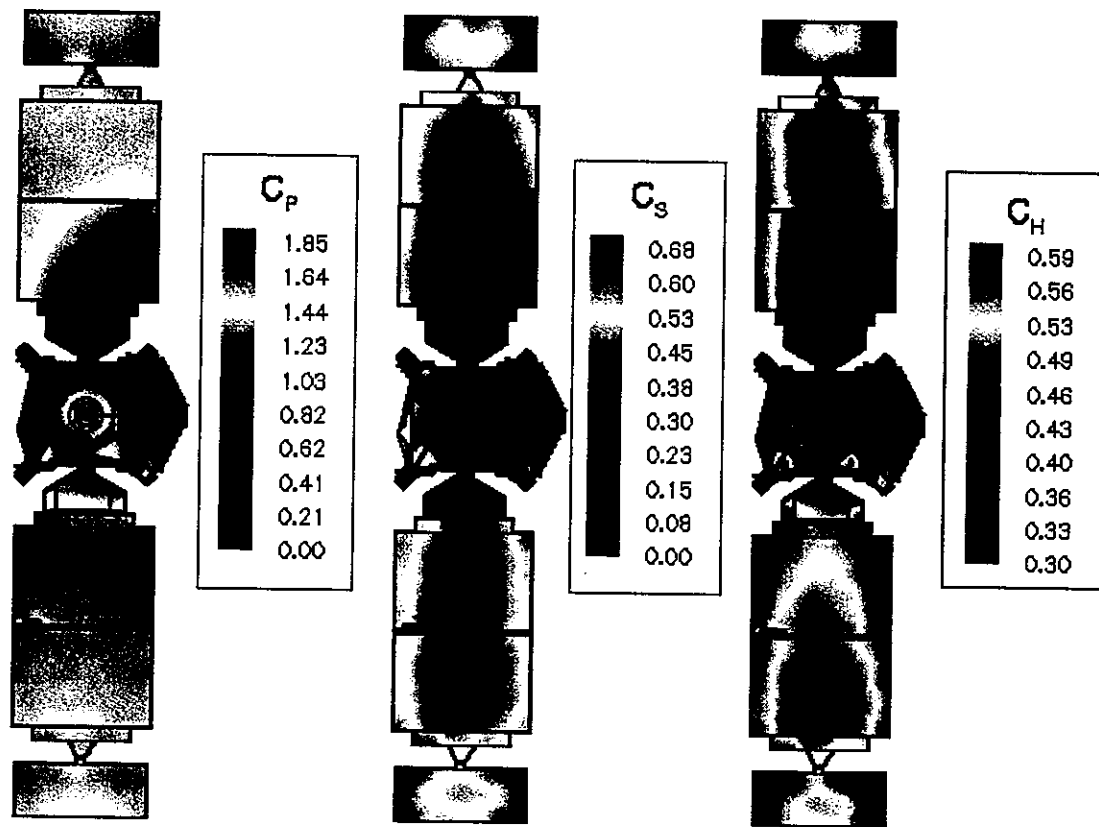


Figure 7.2. Density contour plot of aerobraking configuration with thruster firing.



Angle of Incidence = 0°
 $\rho = 120 \text{ kg/km}^3$

Figure 7.3. Pressure, shear, and heat transfer contours of aerobraking configuration with thruster firing.

ρ [kg/km ³]		Δ Drag [N]	Δ Lift [N]	Δ Yaw [N m]	M_x , array	M_x , total	C_{Mx}	C_{My}
40	Yoke	-0.35	0.05	0.43	3.31	3.58	4.92E-2	4.8E-3
	Inner Panel	-0.83	0.10	1.78				
60	Yoke	-0.54	0.09	0.65	4.31	4.76	4.35E-2	4.7E-3
	Inner Panel	-1.19	0.18	2.56				
120	Yoke	-1.04	0.24	1.26	5.60	6.53	2.99E-2	4.8E-3
	Inner Panel	-1.95	0.40	4.10				

Reference area = 17.5 m²
Reference length = 9 m

Table 7.1. Drag, lift, and moments for aerobraking with thruster firing.

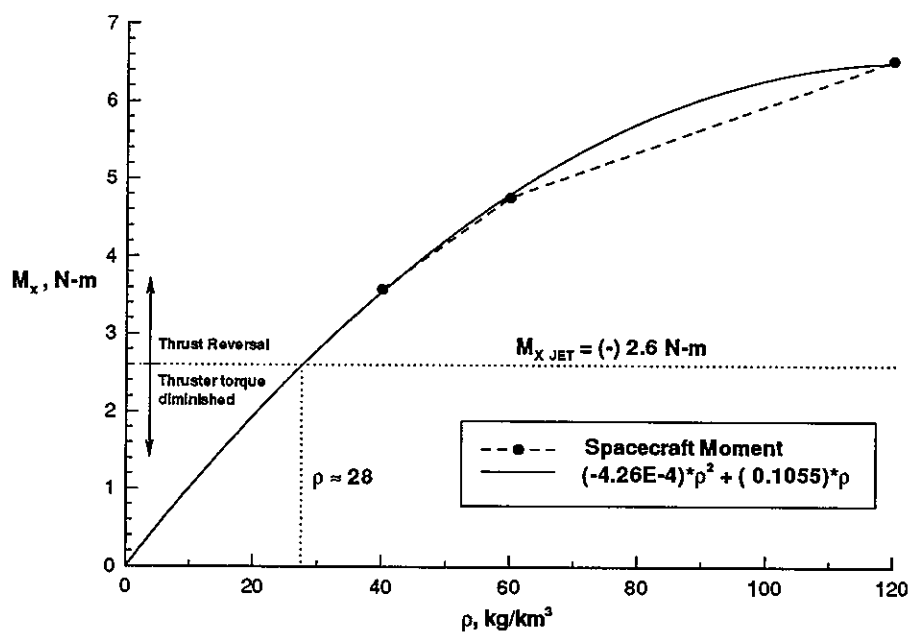


Figure 7.4. Yaw moment variation with density, aerobraking with thruster firing at $\alpha = 0^\circ$

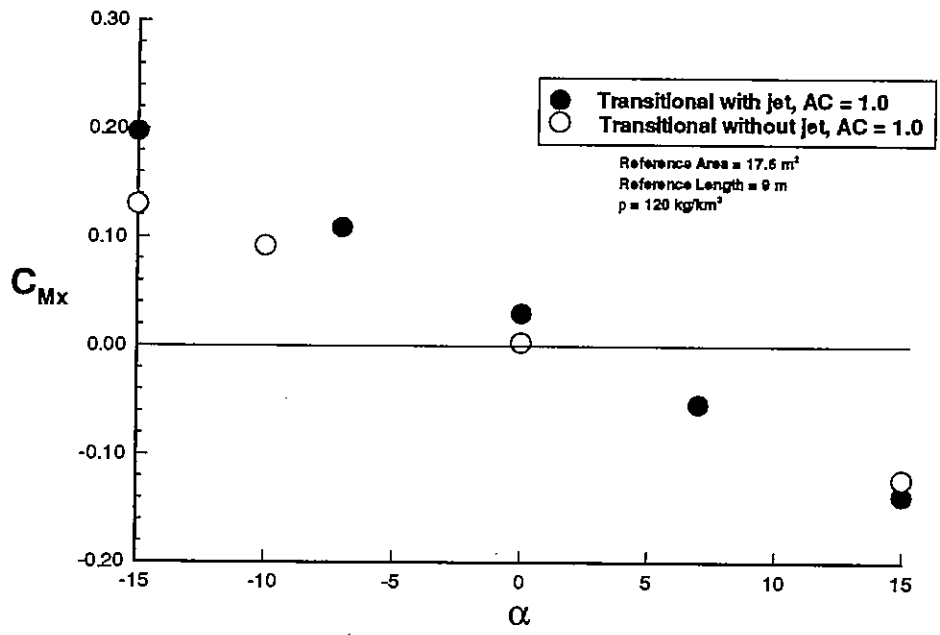


Figure 7.5 Yaw moment coefficient, aerobraking with thruster firing.

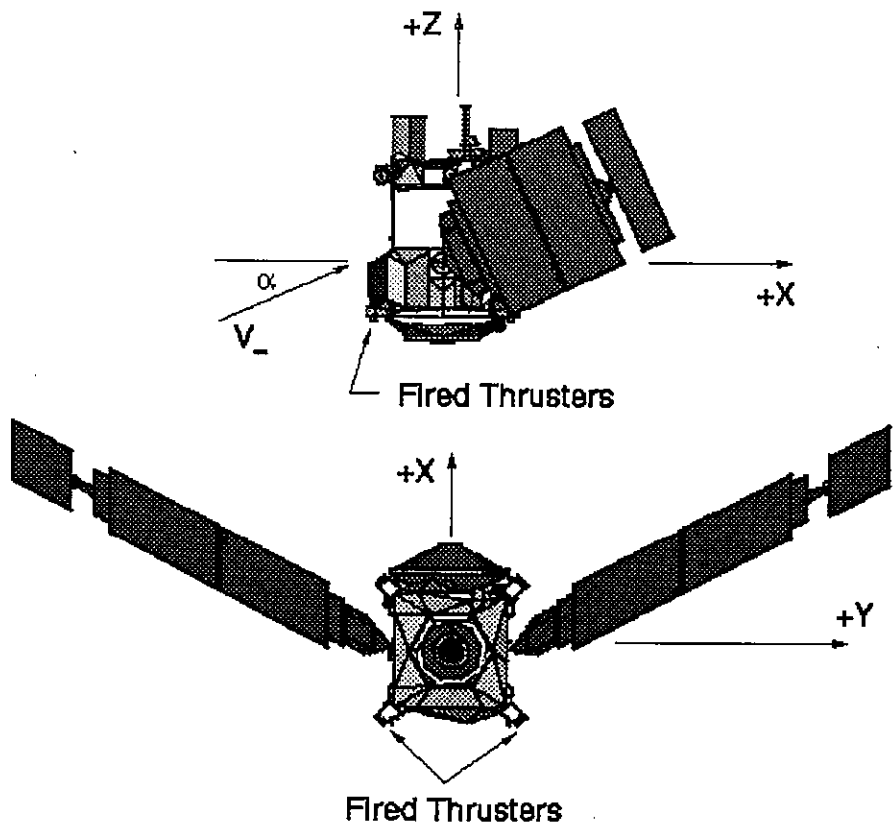


Figure 7.6. Location of simulated thruster plumes, safing configuration.

PRESSURE COEFFICIENT CONTOURS
MGS Safing Configuration

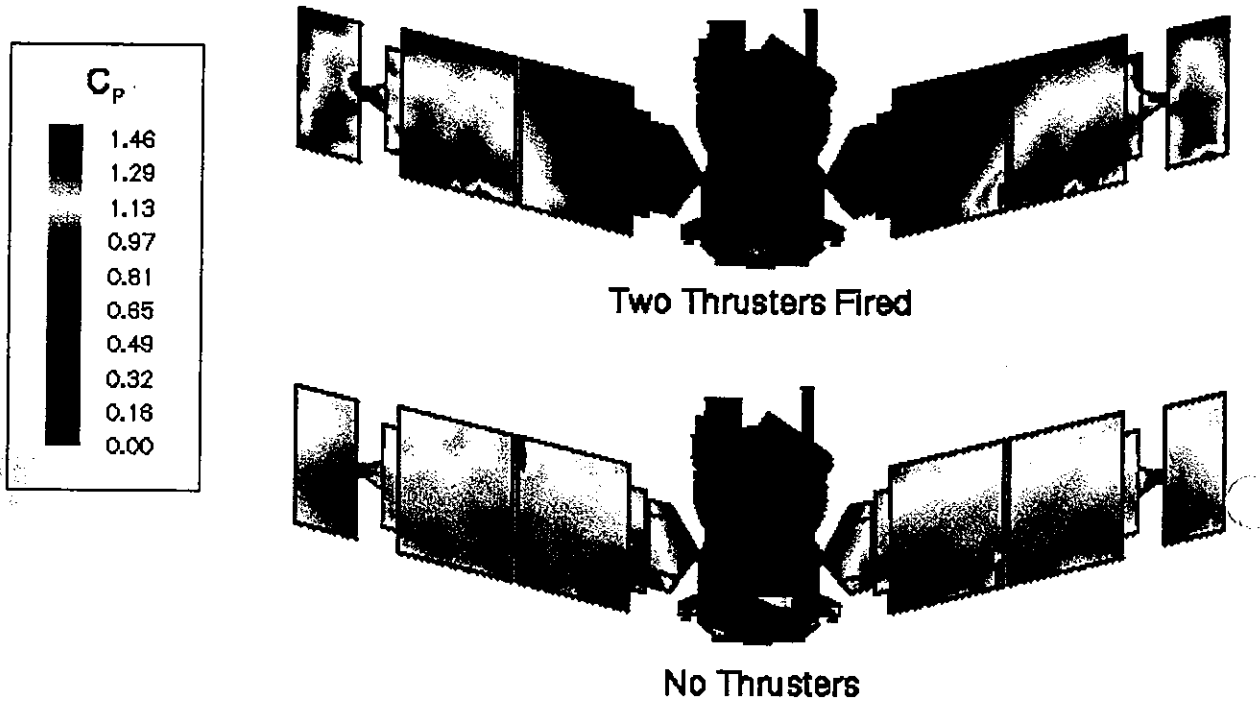


Figure 7.7 Pressure coefficient contours for safing configuration with thruster firing.

HEAT TRANSFER COEFFICIENT CONTOURS
MGS Safing Configuration

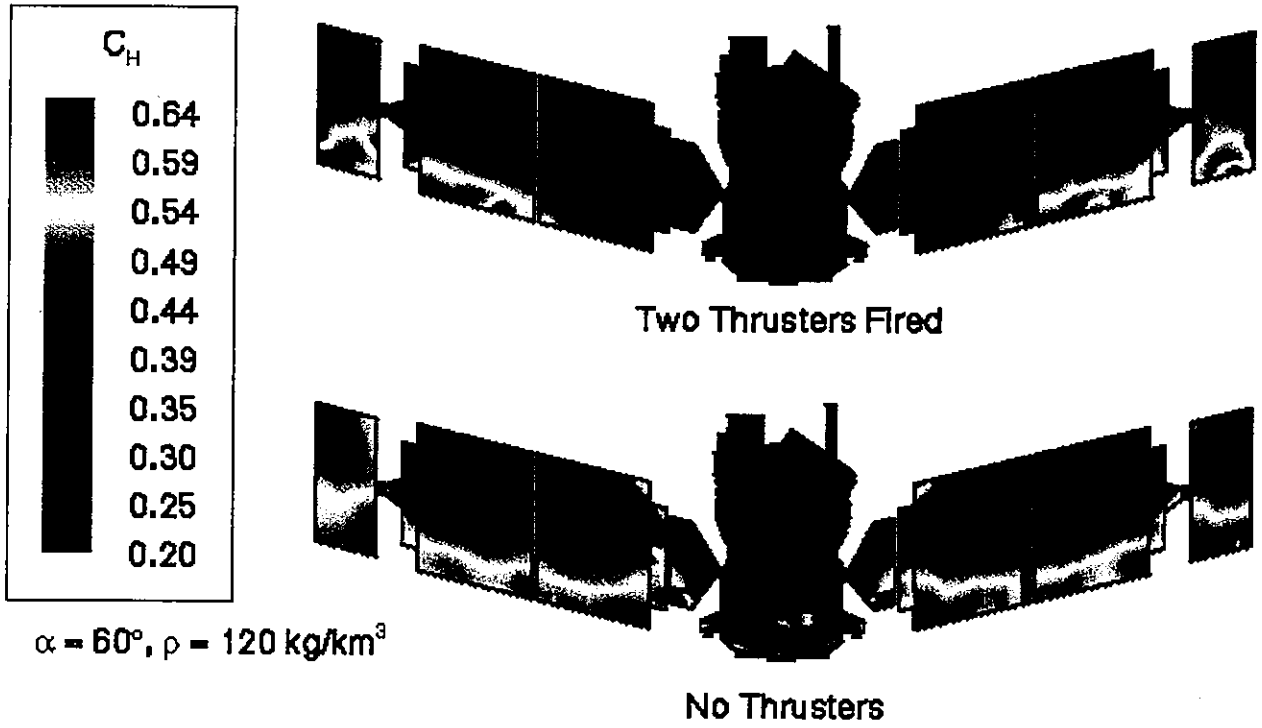


Figure 7.8. Heat transfer contours for safing configuration with thruster firing.

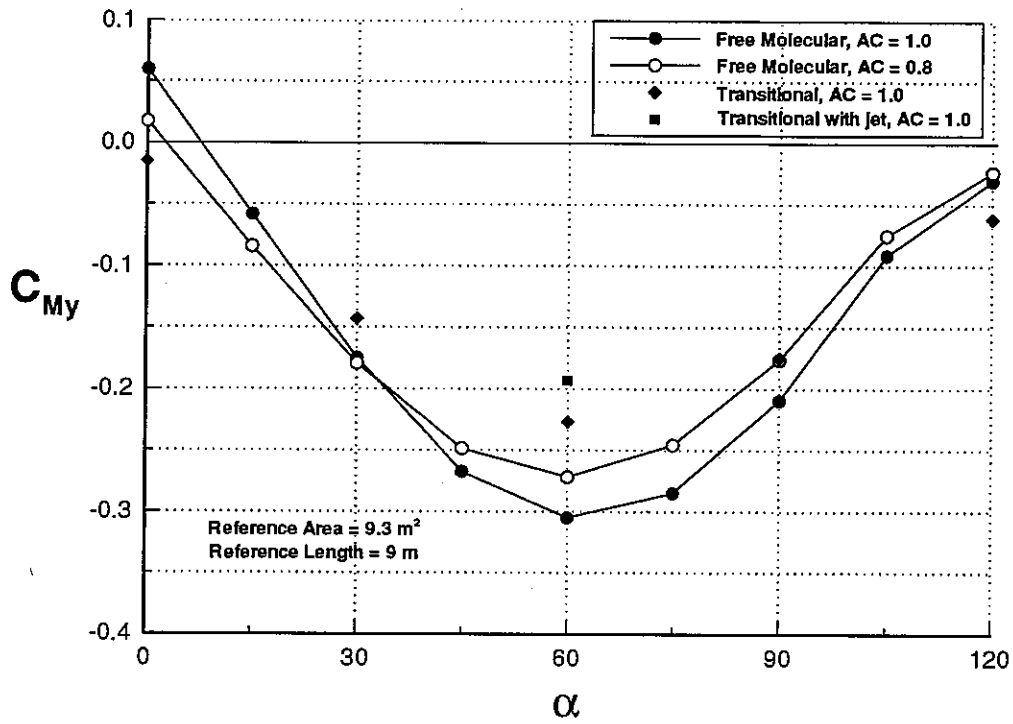


Figure 7.9. Pitching moment coefficient, safin configuration with thruster firing.

APPENDIX A: Computational Tools

Free Molecular Model

Aerodynamic coefficients for the MGS spacecraft in a free molecular flow regime were obtained with two analytical codes - FREEMAC² and Freemol⁵. Both use the same analytical equations but differ in the manner in which the spacecraft is discretized.

FREEMAC uses six fundamental shapes to define a body: rectangular plate, circular plate, triangular plate, circular cylinder, circular cone, and sphere. The spacecraft model consisted of thirty-eight of these components. Freemol uses the same geometry definition that is employed in the DSMC code, as discussed in the next section.

In FREEMAC and Freemol, each elemental surface area of the spacecraft is viewed as a flat plate. The non-dimensional pressure and shear contributions from each elemental plate are⁷:

$$\begin{aligned} \frac{P}{P_\infty} &= \left[\frac{(2 - \sigma_n)S\varepsilon_x}{\sqrt{\pi}} + \frac{1}{2}\sigma_n\sqrt{\frac{T_w}{T_\infty}} \right] \exp(-S^2\varepsilon_x^2) + \\ & (1 + \operatorname{erf}(S\varepsilon_x)) \left[(2 - \sigma_n)(0.5 + S^2\varepsilon_x^2) + \frac{1}{2}\sigma_n\sqrt{\frac{T_w}{T_\infty}}\pi S \cos\theta \right] \quad (1,2) \\ \frac{\tau}{P_\infty} &= \frac{\sigma_t S \varepsilon_y}{\sqrt{\pi}} \left[\exp(-S^2\varepsilon_x^2) + \sqrt{\pi} S \varepsilon_x (1 + \operatorname{erf}(S\varepsilon_x)) \right] \end{aligned}$$

where σ_n and σ_t are normal and tangential accommodation coefficients, respectively; ε_x and ε_y are direction cosines of the freestream with respect to the elemental X and Y axes; S is the speed ratio; and, T_w and T_∞ are the surface and ambient temperatures, respectively. The elemental plate lies in the YZ plane with the X axis pointing in the direction opposite the surface normal (normal points into flow). The speed ratio is defined as the ratio of the freestream velocity V_∞ to the mean molecular velocity,

$$S = \frac{V_{\infty}}{\sqrt{\frac{2kT}{m}}} \quad (3)$$

where k is the Boltzmann constant, T is the temperature of the gas, and m is the molecular mass. Pressure and shear values are then integrated over the whole body to compute total forces and moments. Only the plates facing the freestream contribute to the total aerodynamic force on the spacecraft.

Transitional Model

Results for the transitional flow regime were obtained using the LaRC 3D DSMC computer algorithm. Details of the code and its implementation follow herein.

LaRC 3D DSMC Algorithm

The LaRC 3D DSMC computer code (X2 code) models the freestream gas as a collection of molecules and tracks a representative sample through intermolecular collisions and collisions with the spacecraft surface. As the molecules progress throughout the domain, each molecule's energy, momentum, and location is retained in a file to be used in the next collision and in later post-processing. Key parameters in performing the simulation are FNUM and DTM.

The variable FNUM represents the ratio of the number of real molecules to simulated molecules, and was typically of order 10^{14} - 10^{15} . The simulations averaged 700,000 to one million simulated molecules per domain. The freestream density can be specified and is used together with FNUM to simulate the actual freestream mass density throughout the computational domains. The time step DTM was of the order 0.5 - 1.0e-5.

For each time step, collision partners are determined at the cell level. The location of a molecule within the cell is not important in choosing a collision partner; instead, collision partners are chosen using a probability function. Collisions then take place

according to the VHS molecular model and the Larsen-Borgnakke phenomenological model. In the latter model, all collisions are treated as inelastic, but the proportion of the energy in the collision pair that participates in the energy exchange is restricted⁸. At the end of every other time step, macroscopic properties are sampled for each cell.

Molecules are also exchanged between inner and outer domains. The ability to run each domain on a separate processor is obtained by ensuring that the ratio FNUM/DTM is the same value for both domains to conserve fluxes. This maintains the consistency of the simulation between domains¹³.

The X2 code can also be used to obtain free molecular results. In this case, the code is set so that intermolecular collisions are prevented. Free molecular values from this method compare to analytical results to within 3%.

All DSMC cases were run with an accommodation coefficient of 1.0 and spacecraft surface temperature of 300 K.

Geometric Model

The three dimensional spacecraft model was generated from the geometry of a TRASYS model. TRASYS is software used to perform thermal analyses and models used in it are usually highly detailed. This geometry was chosen since it gives an accurate representation of the spacecraft; it includes all of the instruments, thrusters, and even some thermal blankets.

This model was discretized into a geometry definition appropriate for the DSMC code using shapes categorized as either *quadrics* or *planes*. A quadric is a geometric element that can be described by a quadratic function and is handled analytically by the DSMC code. Typical quadrics are plates, cylinders, cones, and spheres. Other planar surfaces whose limits cannot be adequately described by quadrics are called planes and are stored as a number of points with high resolution¹³. Common planes are rings and disks. The model employed for the MGS spacecraft employed 395 quadrics and 56 data planes.

Computational domain

The simulations are performed using two computational domains. The inner domain just encloses the spacecraft, while the outer domain extends into the upstream and downstream directions. Figure A.1 shows a typical domain configuration. The inner domain size is 3.7 m x 13 m x 5.3 m; the Y dimension is the largest due to the size of the solar panels.

The freestream originates in the outer domain. The position of the inner domain relative to the outer is adjustable - it could be centered or off-centered. Off-centering to the right would create more computational volume for plume development, while skewing the inner domain to the left would leave more space for wake development.

Most of the simulations took place on a multi-processor Sun SPARC workstation. A processor was assigned to each domain; that particular processor would then perform all of the computations relative to that domain. Parallel Virtual Machine (PVM) software¹⁴ was employed to run the computational domains in parallel and allow communication between the two domains.

The volume of the computational domain is discretized using an unstructured grid superimposed onto a uniform Cartesian mesh. Each cell in the mesh is a cube, or pixel. A computational cell in the unstructured grid is typically made of several pixels. A cell where high flow resolution is needed, e.g., near the body, would contain many more pixels than a cell where low resolution is desired, such as far upstream. Discretization of the body replaces the body surface with pixels. Simulations that were performed used about 30,000 cells and 400,000 pixels, on average. Body resolution was on the order of an inch.

Diagnostics

While running the DSMC code, it is necessary to make sure that certain parameters are of the appropriate order to ensure that the simulation gives reasonable results and that the flow is properly resolved in the grid. Three of these parameters are the *numbers of*

molecules/sample, cell size/mean free path, and mean number of molecules/cell. Molecules per sample refers to a running total of the number of molecules in a computational cell that are sampled for properties such as energy and momentum. Values used as a guideline were 10,000 - 100,000 molecules/sample, 10-30 molecules/cell, and a cell size about one third that of the mean free path.

Molecular number density contours were also generated to check the code. Density contours are a quick and effective tool to visualize the structure of the flow field. Typical contours showed a steady increase in density as the panel surface and main body were approached from the upstream, and a very low level immediately downstream of the panels and body. The three parameters discussed above reflected this trend.

The mean number of molecules/cell grew larger than 30 as the body was approached, and number of molecules/sample increased yet most remained within 100,000. The cell size to mean free path ratio grew above 0.33 due to a decrease in mean free path. Ideal values could be achieved with grid adaptation. Experience with the X2 code has shown that adaptation would give a 3-5% refinement in aerodynamic variables.

Convergence Criteria

A DSMC simulation does not stop when a "solution" is obtained. Rather, the simulation can continue indefinitely and is only stopped when various parameters are determined to have converged to some value. A standard deviation of 1-2% over time was considered to be a reasonable criteria for "steady state".

Convergence of aerodynamic variables such as C_D , C_L , and C_M typically took about 3000 time steps, or 20 CPU hours. Convergence of variables related to surface properties in which sampling size is critical, such as C_H , employed considerably more time. A range of 60-80 CPU hours was usually sufficient to obtain a good sampling of molecular collisions with the surface. Resolution of the cells on the body surface was also an important factor in obtaining a good distribution of heat transfer.

Xv.DAT is a file that is periodically updated and stores simulation information such as molecular energies. It is used in obtaining aerodynamic forces, among other values, during post-processing. For example, pressure values that are stored in this file are averages over time of every instance the value is calculated. This means that values at the very start of a simulation would influence the final result. One method used to avoid this was to stop the code and restart after steady state to refresh all counters.

The values of the parameters are reset, yet the molecular field is retained so that the state of the simulation is not lost. This procedure is performed so that final values are taken from a converged simulation and do not include values from earlier times when the variables are still changing significantly with time.

The X2 code generates a diagnostic file which includes the following variables as functions of time: NM , C_D , C_L , C_M , C_H , SAMP, and L/D . Some examples of parameter variation from start to convergence can be seen in Figures A.2. - A.6.

Figure A.2a shows the parameter NM before steady state is reached. NM represents the normalized number of simulated molecules. NM reaches steady state in about ten hours. Figure A.2b shows the variation of this fraction during steady state; it varies less than 0.2% over time. This parameter, taken with others, is usually a good indication that the molecular flow field is well established.

Figures A.3a and A.3b contain plots of C_D variation before and at steady state. Drag coefficient varies by no more than 0.1% throughout steady state. Figures A.4a and A.4b contain the same plots for C_L ; C_L does not deviate by more than 2% from the mean during steady state. The noise is larger for lift coefficient because these values are very small to begin with. Lift to drag ratio L/D in Figure A.5 varies less than 1%. Lift and drag parameters usually took longer to reach steady-state than NM .

Figures A.6a and A.6b show variation of SAMP with CPU time. SAMP represents the total molecular collision rate with the spacecraft surface. This parameter takes almost thirty hours to reach steady-state, then deviates by about 2% throughout this

period. This parameter, if considered together with the surface cell resolution, is important in determining how much time to allow for good surface property resolution.

Post-processing

At the completion of a simulation, post-processing of the data was performed. Forces and moments were found by integrating pressure and shear contributions from surface cells over the spacecraft area. Pressure, shear, and heat transfer coefficient contours were also generated and analyzed.

As mentioned earlier, C_H accuracy is highly dependent on surface collision rate (which is proportional to simulation time) and surface grid resolution. For this reason, post-processing for these values must be done with care. The code that generates surface property values throughout the spacecraft surface can be set to perform "filtering" of values. Filtering consists of averaging C_H , for example, over a designated number of surface pixels. The higher the filter, the greater the number of pixels used for averaging and thus smoother results. However, important information can be lost by using too high a filter.

A relatively high filter was used to generate contour plots whose purpose was to show general heating trends. A lower filter was used if contour lines were to be generated. Zero filter was chosen if C_H variation along a panel diagonal was desired. Scatter of values was always inherent with this method. The software Tecplot (a commercial two and three-dimensional graphical program developed by AMTEC) was used to curve fit polynomials to such data.

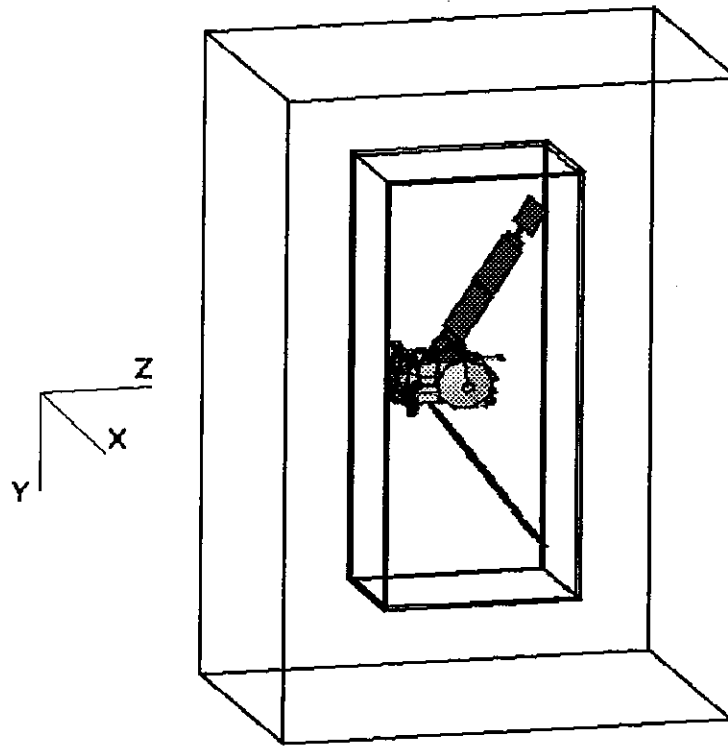


Figure A.1. Inner and outer computational domains with spacecraft model.

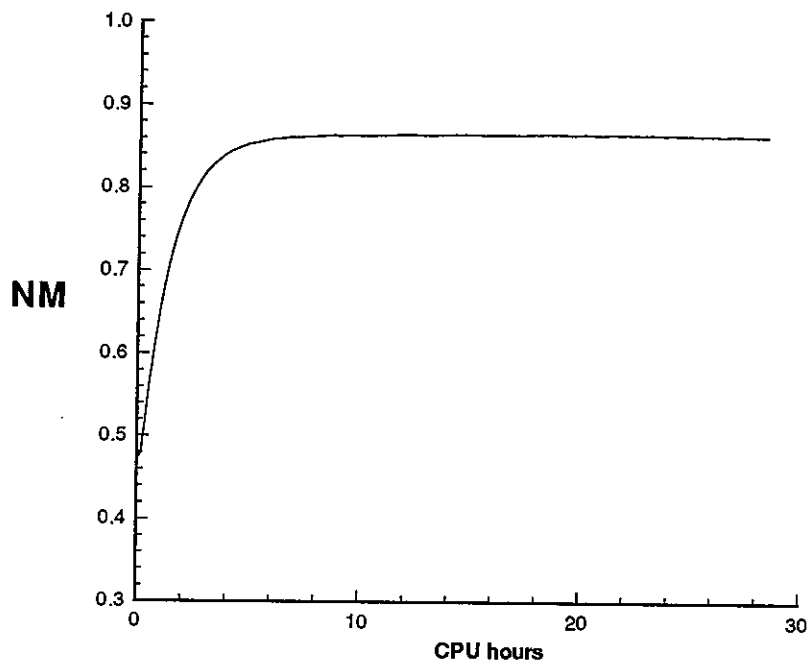


Figure A.2a. Normalized number of molecules before steady state.

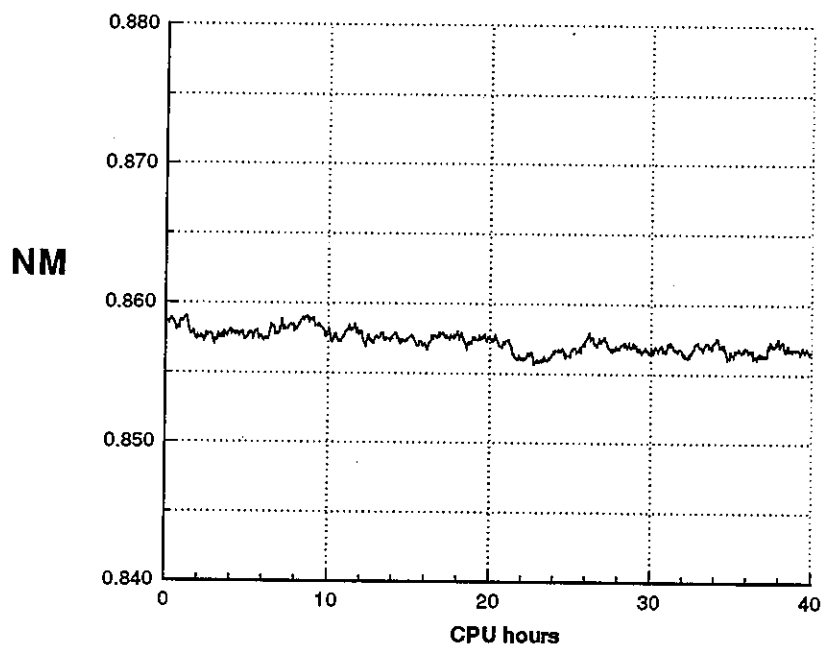


Figure A.2b. Normalized number of molecules at steady state.

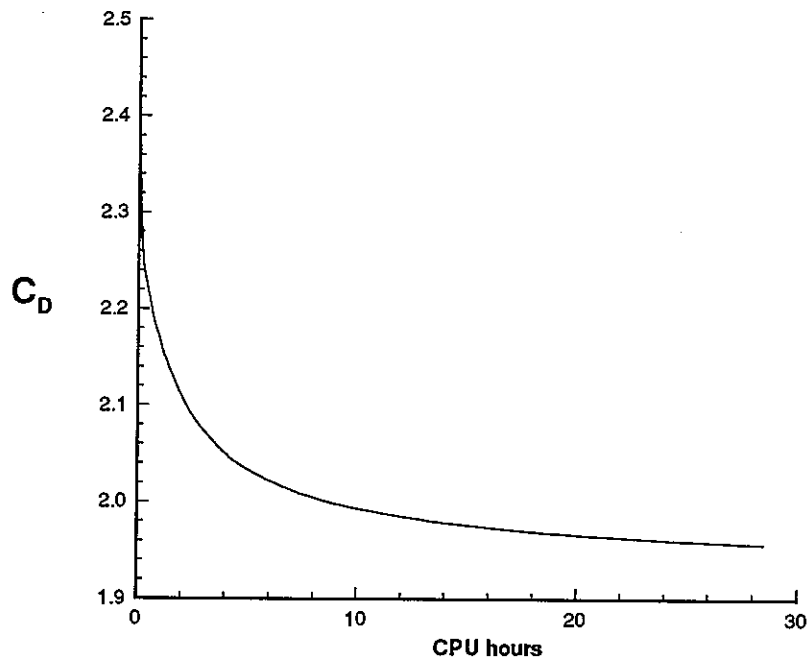


Figure A.3a. Drag coefficient before steady state.

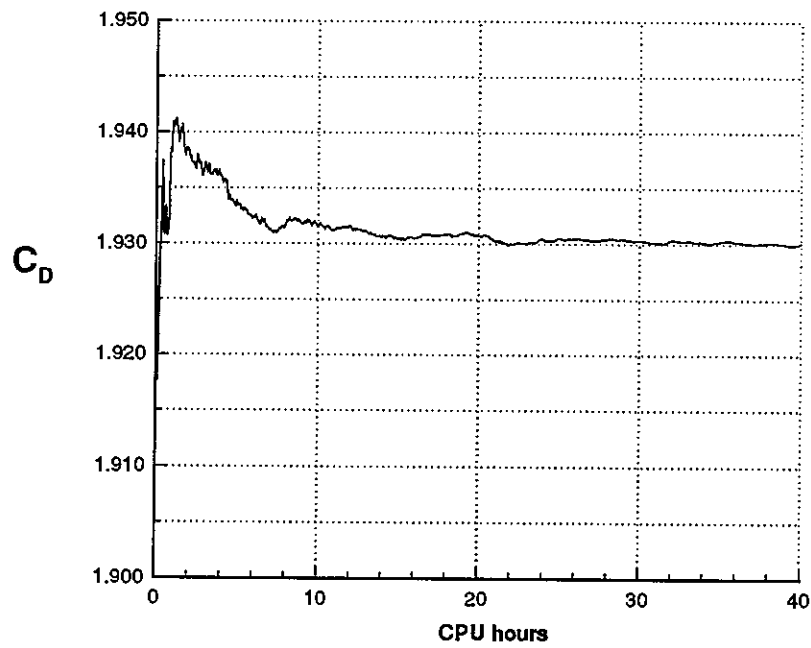


Figure A.3b. Drag coefficient at steady state.

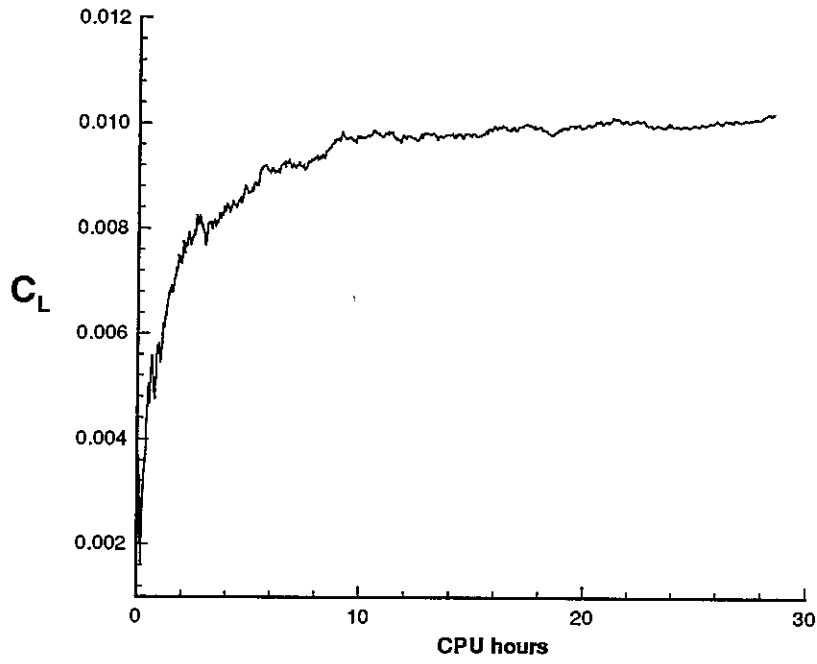


Figure A.4a. Lift coefficient before steady state.

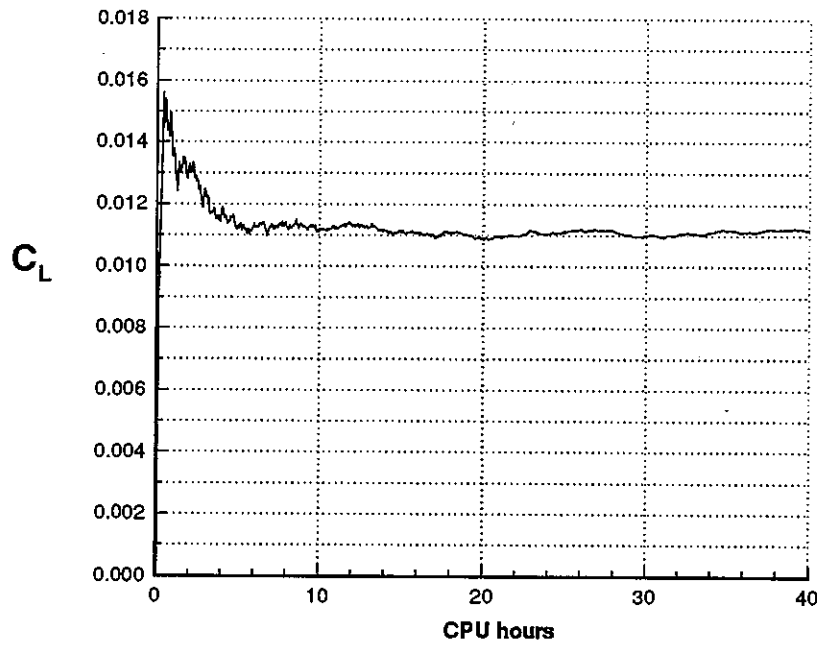


Figure A.4b. Lift coefficient at steady state.

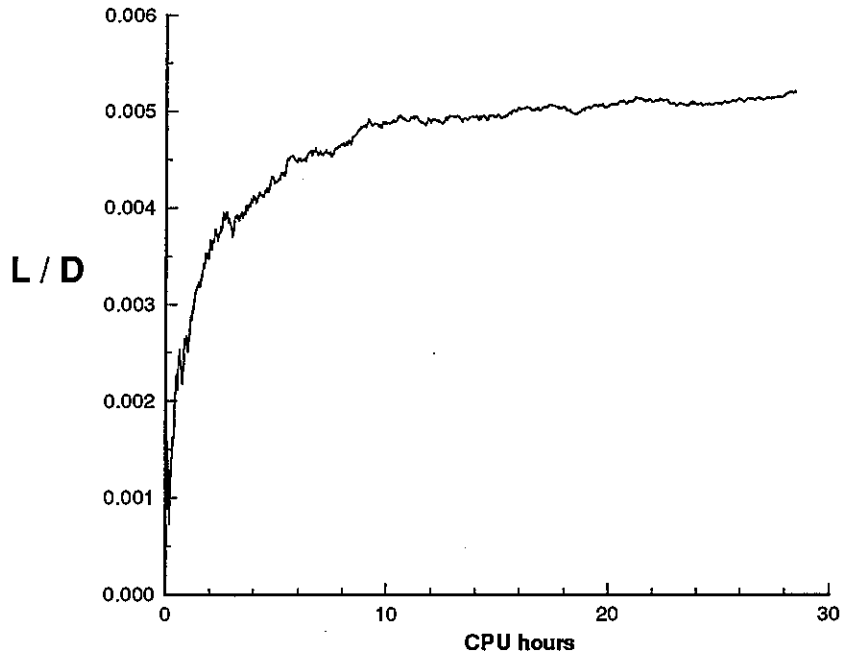


Figure A.5a. Lift to drag ratio before steady state.

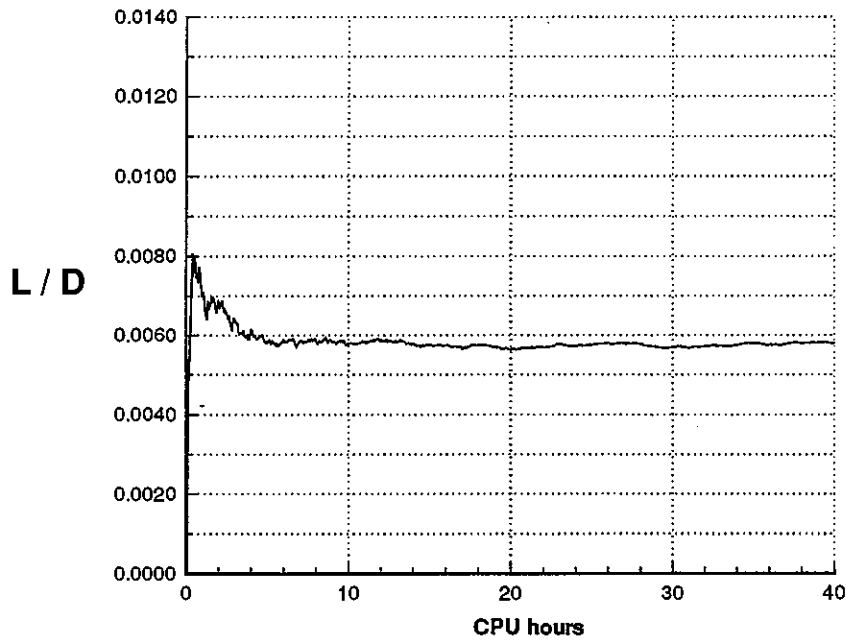


Figure A.5b. Lift to drag ratio at steady state.

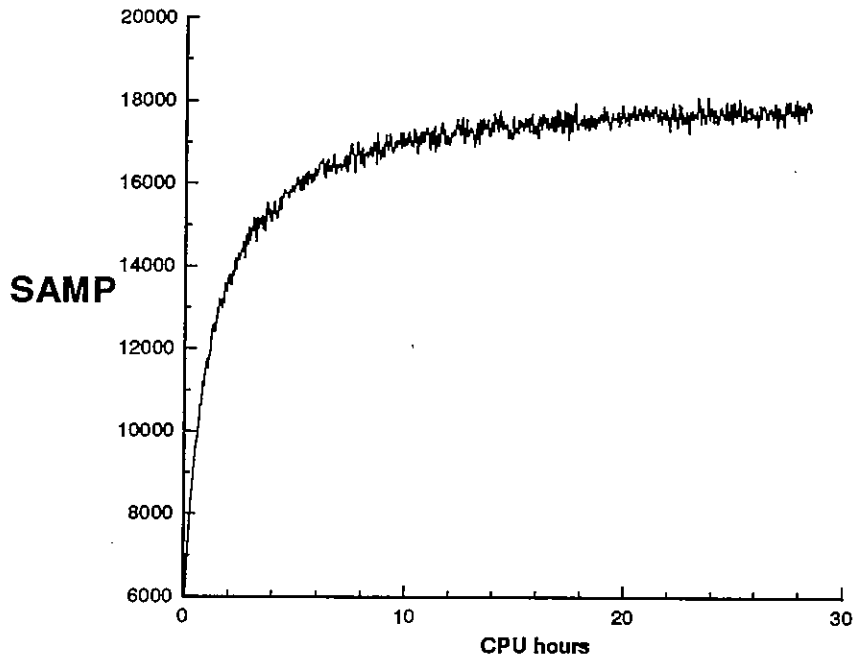


Figure A.6a. Surface collision sampling (proportional to number flux of incident molecules) before steady state.

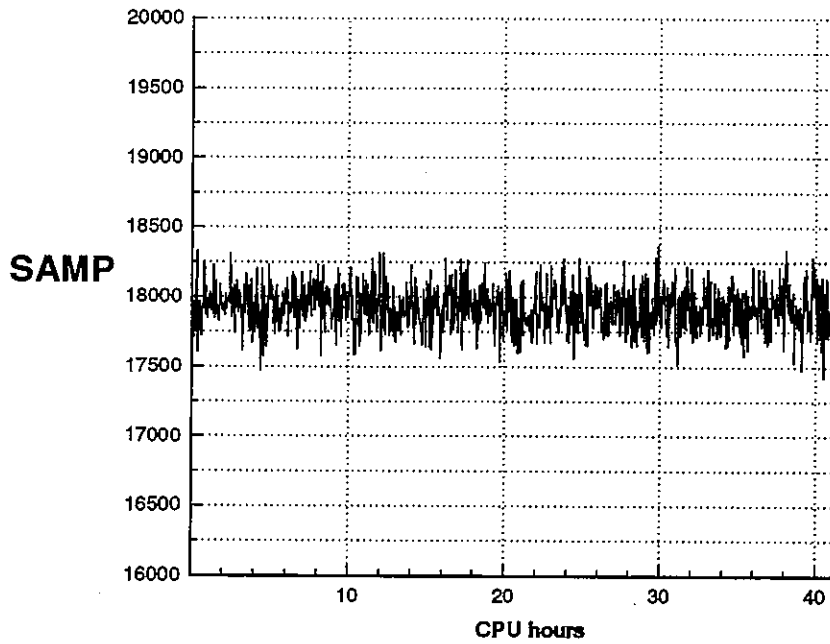


Figure A.6b. Surface collision sampling (proportional to number flux of incident molecules) at steady state.

APPENDIX B: Simulation of Gas Characteristics

Freestream gas properties of Mars atmosphere at nominal periapsis

Composition: 95.5% CO₂, 2.7% N₂, 1.6% Ar, 0.2% O₂ per mole

Nominal density = $8.3e+17$ molecules/m³

Molecular diameter at 1000K reference temperature (Angstroms): 4.18 for CO₂, 3.70 for N₂, 3.34 for Ar, 3.49 for O₂

Variable Hard Sphere (VHS) coefficient: 0.80

Temperature: 148 K

Nominal Velocity: 4811 m/s

Thruster plume characteristics:

The molecular velocity distribution for the plume was represented by a drifted Maxwellian velocity distribution with the following characteristics:

Mean velocity: 2227 m/s with velocity vector linearly varying from 2227 m/s at 0° to 0.0 m/s at 15°

Composition: 48% H₂, 30% N₂, 22% NH₃

Nominal density: $1.82e+23$ molecules/m³ across exit plane of 0.0076 m radius

Molecular diameter at 1000K reference temperature (Angstroms): 2.04 for H₂, 4.15 for NH₃